Targeting of the nuclear RNA exosome to chromatin by HP1 affects the transcriptional programs of liver cells.

Hiba SOUAIFAN 1,4, Mickael COSTALLAT 1, Laura SITKIEWICZ 2, Kylian GODEST 3, Florence CAMMAS 2, Carl MANN 3, Christian MUCHARDT 1*, Christophe RACHEZ 1*

1. Institut de Biologie Paris-Seine (IBPS), Sorbonne Université, CNRS UMR7238, 75252 Paris, France
2. Institute of Human Genetics, CNRS UMR9002 University of Montpellier, 34396 Montpellier, France
3. Institut de Biologie Intégrative de la Cellule (I2BC), CEA, CNRS, Université Paris-Saclay, 91190 Gif-sur-Yvette, France
4. Ecole doctorale Complexité du Vivant, Sorbonne Université, Paris, France
* Co-corresponding authors.
email: christian.muchardt@sorbonne-universite.fr; christophe.rachez@sorbonne-universite.fr

Abstract

HP1, a hallmark of pericentromeric heterochromatin, is a chromatin-bound regulator of co-transcriptional processes including alternative splicing, but its role in RNA degradation remains unexplored. Here, we uncover a direct interaction between HP1 and the RNA exosome, a major RNA decay complex. In mouse embryonic liver cells, inactivation of all three HP1 isoforms led to accumulation of retrotransposon-derived RNAs and stabilization of enhancer RNAs. These changes coincided with increased activity at a subset of liver enhancers particularly sensitive to reduced exosome activity, many of which regulate genes encoding extracellular matrix components such as *Col6a1* and *Col6a2*. Stratifying hepatocellular carcinoma samples by HP1 expression further revealed that tumors with low HP1 were marked by reduced RNA degradation, and increased expression of a similar subset of genes encoding extracellular matrix components and possibly contributing to tumor stiffness. These results suggest that HP1's impact on RNA turnover contributes to its function in cancer biology.

Introduction

Chromatin structure is a major regulator of transcription. This regulation is mediated by molecular machineries that establish transcriptionally active or repressed chromatin states, known as euchromatin and heterochromatin, respectively. In active regions, chromatin influences gene expression programs that govern processes ranging from development to responses to external stimuli. In contrast, constitutive heterochromatin is typically found at pericentromeric regions and transposable elements, and is enriched with repressive epigenetic marks— notably di- and tri-methylation of histone H3 on lysine 9 (H3K9me2/3). These marks serve as binding sites for HP1 proteins, which are essential for the establishment, maintenance, and propagation of heterochromatin [1].

The three mammalian HP1 isoforms—HP1α, HP1β, and HP1γ—share a conserved structure consisting of two globular domains separated by an intrinsically disordered hinge region. The N-terminal chromodomain specifically recognizes and binds H3K9me2/3-marked nucleosomes, anchoring HP1 to heterochromatic regions [2-4]. The C-terminal chromoshadow domain mediates dimerization and interactions with a broad range of PxVxL motif–containing proteins involved in transcriptional regulation, DNA replication, and repair [5,6]. The unstructured hinge region has an affinity for nucleic acids [7]. In addition to their well-established role in heterochromatin, HP1 proteins also localize to actively transcribed genes in both *Drosophila* and mammals, with isoform-specific patterns [8-10]. In euchromatin, HP1 proteins have been implicated in several co-transcriptional processes, including the regulation of alternative splicing [11-15], recruitment of RNAi machinery to chromatin [12], and control of transcriptional elongation [16] and termination [17].

Multiple lines of evidence indicate that the RNA-binding activity of HP1 proteins underlies their functions in both euchromatin and heterochromatin. In both compartments, HP1 proteins engage with repeated RNA sequences. This was first demonstrated by the requirement of RNA binding for HP1 targeting to heterochromatin [18,19]. Later, it was further shown that HP1α specifically associates with pericentromeric major satellite repeat RNA (SatRNA) [20]. More recently, we showed that HP1γ contributes to splicing precision by recognizing hexameric motifs enriched in intronic SINE elements, supporting intron–exon discrimination and contributing to accurate splice site definition [21,22]. In *Schizosaccharomyces pombe*, recognition of repeated sequences by the HP1 homolog Swi6 has been further linked to the degradation of satellite SatRNAs, contributing to transcriptional repression beyond chromatin condensation. Two distinct mechanisms may mediate this repression. First, Swi6 is required for RNAi-dependent silencing by directing SatRNA to the RITS complex, enabling siRNA production via double-stranded RNA formation [23]. Second, silencing at centromeric repeats and the silent mating-type locus—both heterochromatic regions—also involves polyadenylation-dependent RNA degradation via the RNA exosome cofactor Cid14 [24]. Swi6 then engages in a dynamic exchange between free, chromatin-bound, and RNA-bound states, facilitating the delivery of repeat-derived RNAs to degradation machineries [25].

The RNA exosome complex is a central machinery for RNA degradation and quality control in eukaryotic cells [26]. Its core structure consists of nine non-catalytic subunits (Exosc1–9) that form a scaffold for associated 3′→5′ ribonucleases. In the cytoplasm, the exosome partners with

the ribonuclease Dis3l and cytoplasmic cofactors to form the SKI complex, which mediates mRNA turnover and surveillance [27]. In the nucleus, the exosome associates with two ribonucleases: Rrp6/Exosc10, a distributive exonuclease, and Rrp44/Dis3, a processive exo- and endonuclease. The nuclear exosome functions within specialized complexes—NEXT, PAXT, and TRAMP—that provide substrate specificity across a broad spectrum of nuclear RNAs [28]. The TRAMP complex, well characterized in *S. cerevisiae*, contributes to ribosomal RNA processing and snoRNA precursor degradation. In mammals, however, TRAMP is primarily restricted to the nucleolus [29]. By contrast, the NEXT complex targets unprocessed RNAs with a free 3′ end, such as promoter-upstream transcripts (PROMPTs), uaRNAs, and enhancer RNAs (eRNAs) [30-32], while the PAXT complex directs degradation of polyadenylated nuclear RNAs [33]. A defining feature of all exosome complexes is the presence of an RNA helicase. In the cytoplasm, this activity is provided by Ski2, while in the nucleus, Mtr4 is essential for substrate recruitment to NEXT, PAXT, and TRAMP (reviewed in [34]. Recruitment of these nuclear complexes is further mediated by the cap-binding complex (CBC), which recognizes the 5′ methyl-guanosine cap of RNA polymerase II transcripts. CBC, along with its cofactor ARS2, connects to NEXT via the zinc-finger protein ZC3H18, forming the CBC–NEXT axis [35]. ZC3H18 bridges the 5′ cap to the exosome, facilitating the degradation of unstable or aberrant RNAs.

The activity of the RNA exosome has previously been linked to the organization of chromatin structure. At a large scale, chromatin architecture, particularly topologically associating domains (TADs) and chromatin loops, is shaped by architectural proteins such as CTCF and cohesins [36]. Depletion of the nuclear exosome subunit DIS3 impairs non-coding RNA processing, reduces CTCF binding, and disrupts TAD organization at the *Igh* locus [37]. In parallel, transcripts derived from normally silenced retroelements are targeted for degradation by the NEXT complex, which recognizes unstable RNAs arising from heterochromatic regions [38,39]. Mass spectrometry (MS) approaches have finally suggested that RNA exosome-associated factors such as ZC3H18 and the RNA helicase MTR4 may associate with HP1 [40,41], while, reciprocally, HP1 MS data has detected ZC3H18 among the interacting partners of all three HP1 isoforms [42]. This association suggest that molecular bridges may exist between chromatin, HP1, and nuclear RNA degradation machineries.

Building on this possible connection, we have here analyzed the relationship between chromatin-associated HP1 proteins and RNA exosome components in murine BMEL liver cell lines depleted of all three HP1 isoforms. Previous studies using these cells showed that HP1 depletion results in the accumulation of transcripts from normally silenced retroelements, including LINEs, SINEs, and LTR-containing endogenous retroviruses (ERVs) [43,44]. In this context, we confirm physical associations between HP1 proteins and several representative components of the nuclear exosome, and show an HP1-dependent enrichment of exosome complexes at chromatin loci. HP1 loss also led to a marked increase in chromatin-associated unstable transcripts, such as PROMPTs and retroelement-derived RNAs, particularly at LTR loci. Notably, some of these transcripts extended beyond the annotated repeat boundaries and were detected in a mature form in the cytoplasm. In parallel, enhancers located near these retroelements became activated in the absence of HP1, leading to upregulation of adjacent genes and widespread alterations in transcriptional programs.

Results

HP1 proteins interact with components of the RNA Exosome and affect their subcellular localization.

Analysis of ZC3H18 immunoprecipitation–mass spectrometry data [41] using the STRING database (Search Tool for the Retrieval of Interacting Genes/Proteins) documented that the protein-protein interactions linking the RNA exosome and the Cap binding complex with the three HP1 proteins and other epigenetic regulators, were supported by multiple independent sources (Fig. 1A, each "string" represents a documented protein-protein interaction). This prompted us to further investigate the links between HP1 proteins and the nuclear RNA Exosome.

To this end, we compared mouse embryonic liver (BMEL) cells lacking all three HP1 isoforms (triple knockout, TKO) to HP1-expressing controls (Het, heterozygous for HP1α and wild type for HP1β and HP1γ). Six independent clones were analyzed: TKO1, TKO2, TKO3, and Het1, Het32, Het35 (Fig. 1B and Supplementary Fig. 1A). Western blot analysis of total extracts showed that protein levels of EXOSC3 and EXOSC9 (core exosome subunits), MTR4 (a nuclear RNA helicase common to all nuclear exosome complexes), and ZC3H18 (a zinc-finger adaptor protein specific to the NEXT complex) were similar between Het and TKO clones, indicating that HP1 depletion did not affect their overall expression (see representative clones, Fig. 1C). Upon fractionation of the Het clones into cytosolic (C), nucleosolic (N), and chromatin (X) extracts, the four proteins were predominantly detected in the nucleosolic and chromatin fractions, which were also enriched in HP1γ (Fig. 1D). Interestingly, in the TKO clones, we observed increased accumulation of EXOSC9 and EXOSC3 in the cytosolic fraction, suggesting reduced nuclear retention of these subunits (Fig. 1D, lanes C). Fractionation quality was validated by Western blotting for marker proteins and by analyzing the distribution of representative cytoplasmic and nuclear transcripts (Supplementary Fig. 1A–C).

Finally, co-immunoprecipitation from nuclear extracts containing both soluble and chromatin-associated material confirmed an association of HP1 proteins with EXOSC9, EXOSC10, MTR4, and ZC3H18, consistent with the previously reported MS data (Fig. 1E-G and Supplementary Fig. 1D-E). These interactions were maintained following RNase treatment (Supplementary Fig. 1F), indicating that they were not mediated by RNA. Together, these results further documented interactions between the HP1 proteins and components of the RNA exosome machinery, and suggested that these interactions are required for full nuclear retention of certain exosome subunits.

Several non-coding, unstable RNA species are found stabilized in the absence of HP1 proteins, in both chromatin and cytosolic fractions.

We next used RNA-seq to examine RNA profiles in chromatin and cytosolic fractions of the BMEL Het and TKO clones (Fig. 1B). In this setup, the chromatin fraction was expected to be enriched in nascent and incompletely processed RNAs, whereas the cytosolic fraction was expected to be depleted of unstable nuclear transcripts and enriched in mature mRNAs (Supplementary Fig. 1C). In parallel, RNA-seq was also performed on total RNA from each clone. The RNA species we examined included various RNAs encoded by LTRs, LINEs, SINEs, and MMSAT repeats. For these, we focused on extragenic repeat elements, excluding those located within gene bodies, such as intronic repeats, which may be transcribed incidentally as part of

181 coding gene expression and processed in that context. We also examined levels of upstream
182 antisense uaRNA at promoters (PROMPT RNA), and eRNA at active distal enhancers (enhD
183 RNA), all documented as unstable transcripts. Genomic elements were considered as expressed
184 when yielding at least two RNA-seq reads in at least one experimental condition.
185 Using this criterion, levels of unstable transcripts increased in TKO cells compared to HP1-
186 expressing (Het) cells. In particular, we noted that for more than 50% of all expressed LTR
187 elements, expression was detected exclusively in TKO cells (see examples in Fig. 2A, and
188 quantification in Fig. 2B). Several elements were also expressed exclusively in Het cells, reflecting
189 the multiplicity of HP1 functions not solely linked to RNA stability [45]. Global analysis of RNA
190 abundance further showed that mean RNA levels from PROMPTs, distal enhancers (enhD), and
191 repeat elements (LTRs, LINEs, SINEs) were increased in the chromatin fraction of TKO cells
192 relative to Het (Fig. 2C). In contrast, chromatin-associated pre-mRNAs from Ensembl-annotated
193 genes, measured by exonic reads, were less affected by HP1 depletion. Globally, the Ensembl gene
194 transcript category showed more moderate changes in both RNA levels and the number of loci
195 with TKO- or Het-specific expression compared to non-coding RNA categories (Fig. 2E-G). These
196 findings suggest that HP1 loss predominantly affects the expression and/or stability of unstable,
197 non-coding RNAs, rather than processed mRNAs. Supporting this, several non-coding RNAs that
198 accumulated in the chromatin fraction—particularly those derived from LTRs, LINEs, and
199 MMSAT repeats—were also found at higher levels in the cytoplasm of TKO cells (Fig. 2D). In
200 addition, many LTR-initiated transcripts extended for several kilobases and, interestingly, some
201 appeared to be spliced in the cytoplasm (e.g., RLTR17, RMER13A; Fig. 2A), suggesting that in
202 the absence of HP1, these RNAs evade nuclear decay and undergo canonical maturation.
203 Notably, several of the LTR-derived transcripts most readily detected in TKO cells (Fig.
204 2H, green and red profiles) were also reported as overexpressed in a previous study following
205 depletion of ZFC3H1 or ZCCHC8, components of the PAXT and NEXT nuclear exosome
206 pathways, respectively, in mouse embryonic stem cells [38]; Fig. 2H, yellow and light blue profiles).
207 While derived from a different cell type, this overlap supports the idea that the accumulation of
208 LTR transcripts observed in TKO cells reflects impaired exosome-mediated RNA degradation.
209 Together, these results suggest that HP1 loss stabilizes normally unstable non-coding RNAs,
210 possibly due to defective degradation at the chromatin level.
211
212
213 **An HP1-dependent association of nuclear RNA exosome and cofactors to chromatin loci.**
214 Having observed that HP1 inactivation alters the nuclear retention of RNA exosome
215 components and leads to the accumulation of unstable RNAs on chromatin, we next sought to
216 examine more closely how RNA exosome components associate with nuclear structures. We
217 therefore performed chromatin immunoprecipitation followed by high-throughput sequencing
218 (ChIP-seq) with anti-EXOSC10, -ZC3H18, and -MTR4 antibodies using the Het32 and the TKO2
219 clones. To also gain insight in the overall impact of HP1 inactivation on chromatin structure, we
220 completed this series of experiments with anti-CTCF, and anti-phospho RNA polymerase II (P-
221 RNAPII, as a mix of both phospho-Ser2 and -Ser5 forms) ChIP-seq, and HP1α, HP1β, HP1γ,
222 H3K9me3, and H3K27me3 CUT&Tag experiments (Fig. 3A).
223 Examination of the ChIP-seq profiles with a genome browser revealed that the nuclear
224 exosome components, MTR4, ZC3H18, and EXOSC10 are actively recruited to chromatin at
225 specific genomic loci. This recruitment was most clearly detected in regions also recruiting P-
226 RNAPII, while Mtr4 also displayed an interesting overlap with CTCF. Importantly, the chromatin

227 recruitment of exosome components was strongly diminished in TKO2 cells, indicating that HP1
228 proteins are required for their proper localization to these regions. In contrast, levels of
229 phosphorylated RNA polymerase II (P-RNAPII) appeared increased in TKO2 cells (Fig. 3A).
230 Quantification of MTR4, ZC3H18, and EXOSC10 ChIP-seq peaks detected with the MACS2
231 package confirmed a dramatic decrease in the number and/or intensity of these peaks upon
232 inactivation of the HP1 genes, while the total number of P-RNAPII peaks was strongly increased
233 (Fig. 3B-C).
234
235 Metagene analysis on more than twenty thousand genes confirmed a preferential enrichment
236 of MTR4, ZC3H18, EXOSC10 on the body of genes, with a peak at the transcription start site
237 (TSS - Fig. 3D). Thus, the distribution of these factors coincided with that of the P-RNAPII,
238 although missing accumulation at sites of transcription termination (TES). This analysis further
239 revealed that HP1 inactivation led to a uniform reduction in RNA exosome component-occupancy
240 over gene bodies, while RNAPII occupancy was correspondingly increased (Fig. 3D, compare
241 brown and dark blue profiles). CUT&Tag analysis of the recruitment of each HP1 isoform in Het
242 cells showed their preferential enrichment at gene transcriptional start sites (TSS, blue profiles Fig.
243 3E), compared to the background HP1 alpha CUT&Tag signal in TKO cells (orange profile Fig.
244 3E). This distribution of HP1 proteins at actively transcribed genes is consistent with earlier reports
245 [46]. It is also compatible with a co-recruitment of HP1 and RNA exosome proteins at promoter
246 regions. Thus, HP1 inactivation leads to both reduced recruitment of the RNA degradation
247 machinery and increased recruitment of RNA polymerase II, supporting a model in which HP1
248 proteins contribute to gene silencing by simultaneously restricting transcription and promoting
249 RNA degradation. Of note, although HP1 enrichment at TSS was not associated with
250 H3K9me3 or H3K27me3 marks, HP1 colocalized with H3K9me3 at other regions, such as simple
251 repeats (Fig. 3E and 3F, and Supplementary Fig. 3A and 3B). At these sites, HP1 inactivation did
252 not lead to a loss of H3K9me3 but rather to a redistribution of the mark across repeats. These
253 observations suggest that the targeting of the RNA exosome to TSS by HP1 and its association
254 with H3K9me3 at other loci rely on two independent mechanisms.
255
256
257 **HP1 concentrates MTR4 and CTCF at gene promoters.**
258 We next examined in more detail the apparent colocalization of MTR4 with CTCF peaks.
259 Quantification confirmed that 90% of the MTR4 peaks match CTCF peaks (representing
260 approximately 15% of the total number of CTCF peaks). It also showed that MTR4 was the only
261 RNA exosome component under scrutiny to display this colocalization (Fig. 4A). Comparison of
262 ChIP-seq data between Het32 and TKO2 cells showed that the overall number of CTCF peaks
263 remained broadly unchanged following HP1 depletion (Fig. 4B). However, genome browser
264 visualization revealed a redistribution of CTCF binding: in TKO2 cells, new CTCF peaks appeared
265 at previously annotated loci where no binding was detected in Het32 cells, while many pre-existing
266 peaks decreased in intensity, eventually below levels of detection (Fig. 4C). Heatmap analyses
267 confirmed this genome-wide redistribution of CTCF occupancy (Fig. 4D). The genome-browser
268 visualization further suggested that a large fraction of the CTCF peaks colocalizing with MTR4
269 were located at promoters. Sorting promoters according to HP1 occupancy revealed that CTCF
270 and MTR4 were co-enriched at HP1-bound promoters in Het32 cells and that HP1 inactivation led
271 to a strong reduction of both CTCF and MTR4 enrichment at these sites, accompanied by an
272 increase in P-RNAPII signal (Fig. 4E). Together, these results suggest that HP1 proteins contribute

273 to concentrating both CTCF and MTR4 at a subset of promoters, possibly also preventing it from
274 ectopic associating with other CTCF binding sites.
275
276
277 **A gain in chromatin accessibility at enhancers affects collagen gene expression**
278 To gain broader insight into the regulatory elements impacted by HP1 inactivation, we
279 intersected both CTCF ChIP-seq peaks and HP1 CUT&Tag peaks with the catalog of candidate
280 cis-regulatory elements (cCREs) annotated by the ENCODE project (Fig. 5A and Supplementary
281 Fig. 5A). This analysis revealed that CTCF peaks were located within annotated regulatory
282 elements, including promoters and enhancers, both locations where they were mostly lost in the
283 absence of HP1 (Supplementary Fig. 5A). In parallel, approximately 40% of HP1 peaks were also
284 located within promoters as well as enhancers, with a predominance of distal (enhD) versus
285 promoter-proximal enhancers (enhP) (Fig. 5A). To further investigate the consequences of HP1
286 loss on enhancer activity in BMEL cells, we performed ATAC-seq in Het and TKO clones. Based
287 on chromatin accessibility profiles, distal enhancers (enhD) were categorized as active in both
288 conditions, with decreased activity in TKO cells, with increased activity in TKO cells, or inactive
289 (Unchanged, Down, Up, Inactive, respectively. Supplementary Fig. 5B). Heatmap analyses
290 revealed that, similar to observations at promoters, a substantial fraction of active enhancers were
291 associated with HP1 in Het cells (Fig. 5B).
292 Importantly, activation of enhancers upon HP1 inactivation correlated with the upregulation
293 of nearby genes located within 100 kb (enhD Up, orange bar, Fig. 5C). Gene ontology analysis of
294 these upregulated genes revealed a strong enrichment for terms associated with the collagen-
295 containing extracellular matrix (Fig. 5D). Further examination showed that multiple collagen
296 isoforms were specifically upregulated at enhancers derepressed upon HP1 inactivation, as
297 exemplified at the *Col6* locus (Fig. 5E, and list in Supplementary Fig. 5C). This activation
298 correlated with an increased accumulation of transcripts over the enhD elements in the chromatin
299 fraction, and at some loci, also in the cytosolic fraction, suggesting increased stability of enhancer
300 RNAs (eRNAs)—potentially a consequence of the reduced recruitment of RNA exosome
301 components to chromatin (Fig. 5E, arrows; Sup. Fig. 5B). This mechanism may also be at play for
302 the few thousand LTR retroelement transcripts that were stabilized in TKO (Sup. Fig. 5D). These
303 findings suggest that collagen genes are particularly sensitive to decreased RNA exosome activity.
304 To further support this hypothesis, we analyzed publicly available transcriptomic datasets from
305 *Exosc3* conditional knockout mouse embryonic stem cells (GSE100535, Fig. 5F) and HeLa cells
306 depleted of ZFC3H1 (GSE212557, Fig. 5G). Remarkably, in both models, genes associated with
307 the collagen-containing extracellular matrix were among the most significantly affected pathways
308 following disruption of RNA exosome activity.
309
310
311 **HP1 Deficiency and Reduced RNA Exosome Activity Converge to Deregulate Collagen**
312 **Genes in Hepatocellular Carcinoma**
313 To investigate the relevance of HP1–RNA exosome cooperation in hepatocellular carcinoma
314 (HCC), we reanalyzed RNA-sequencing data from a cohort of 76 Mongolian HCC patients [47]. The
315 molecular subtypes identified in this cohort largely mirrored those previously described in patients
316 from other geographic regions, including Asia, Europe, and North America. Our analysis revealed
317 that HP1 gene expression—including CBX3, CBX1, and CBX5—was upregulated in the majority
318 of tumors, with 71% of cases showing at least a twofold increase relative to adjacent healthy tissues

319 (Supplementary Fig. 6A). This observation is consistent with previous reports linking elevated
320 HP1 levels to poor prognosis in HCC (Supplementary Fig. 6B).
321 To examine the consequences of differential HP1 expression, we ranked patients based on
322 cumulative HP1 levels (sum of *CBX3*, *CBX1*, and *CBX5* expression) and stratified them into Hi
323 HP1 and Lo HP1 groups, corresponding to the upper and lower quartiles (Fig. 6A; Supplementary
324 Fig. 6C). This stratification effectively separated the cohort into two subgroups in unsupervised
325 PCA (Fig. 6B). The Hi HP1 group was enriched for patients previously associated with poor
326 prognosis and included a higher proportion of deceased individuals (Fig. 6A; Supplementary Fig.
327 6D–E; ref. 47). Genes upregulated in Hi HP1 tumors were significantly enriched for cell cycle–
328 related pathways (adjusted p-value = 4.87e-14; Supplementary Fig. 6F). These tumors also showed
329 increased expression of the alpha-fetoprotein gene *AFP* and *YAP1*, markers of poorly differentiated
330 and highly proliferative hepatocytes (Fig. 6D, Lo HP1 vs Hi HP1). Together, these data suggest
331 that Hi HP1 tumors are more aggressive, with enhanced proliferation and loss of hepatocytic
332 identity.
333 To estimate RNA turnover in the Lo HP1 group, we quantified the accumulation of unstable
334 mRNAs using the RNA HiLo ratio—a validated proxy for RNA degradation activity [48]. This
335 approach was used because the available transcriptomes lacked sufficient depth to detect rare non-
336 coding RNAs from enhancers or promoters directly. The analysis revealed that labile mRNA
337 species accumulated significantly more in Lo HP1 tumors compared to Hi HP1 tumors, consistent
338 with reduced RNA degradation (Fig. 6C). This accumulation correlated with increased expression
339 of antiviral response genes, including *RIG-I*, *NLRP3*, *ISG20*, and *IRF7* (Fig. 6D, Lo HP1 vs Hi
340 HP1), suggesting activation of an RNA-triggered innate immune response. Supporting this, we
341 observed elevated expression of genes predominantly expressed in immune cells rather than
342 hepatocytes, indicating that the innate immune activation is accompanied by inflammation in the
343 tumor microenvironment.
344 In parallel, GO cellular component analysis identified "collagen-containing extracellular
345 matrix" as the top enriched category (Fig. 6F). This is consistent with our findings in mouse liver
346 cells with reduced RNA exosome activity (Fig. 5D). In Lo HP1 tumors, we also observed increased
347 expression of α-SMA/*ACTA2* and vimentin, markers of activated hepatic stellate cells (HSCs) (Fig.
348 6D). These changes suggest an increased fibrogenic state, in which HSCs secrete extracellular
349 matrix proteins and drive fibrotic remodeling of the tumor microenvironment.
350 An increase in extracellular matrix (ECM) stiffness is a characteristics of tumoral
351 progression of HCC, where increased ECM is preventing immune infiltration in the tumor,
352 allowing HCC to reach more severe stages [49]. Indeed tumor samples compared to their matching
353 non-tumor controls revealed typical high levels of collagen gene expression and low immune
354 response (Fig 6D, tumor vs. non-tumor). However our findings reveal that Lo HP1 tumors promote
355 both a fibrotic evolution and an anti-viral innate immune response affecting the tumor
356 microenvironment (Summarized in Fig. 6G). We state that this immune response is likely to be
357 triggered by the accumulation of undegraded RNA and is key to the better survival of Lo HP1
358 HCC patients. They further imply that the increased expression of collagen-associated genes may
359 be a direct consequence of reduced HP1/RNA exosome activity on chromatin, and that these genes
360 are particularly sensitive to enhancer regulation dependent on chromatin-linked RNA degradation
361 mechanisms.
362

Discussion

We identified an unrecognized role for chromatin-associated HP1 proteins in guiding the nuclear RNA exosome to specific genomic loci. HP1 depletion in BMEL cells led to the accumulation of normally unstable nuclear RNAs, including transcripts from repetitive elements, promoters, and enhancers. The increased production of eRNAs was also accompanied by the activation of a subset of enhancers and the subsequent upregulation of nearby genes, many of which were involved in the extracellular matrix, including several collagen genes. This had important functional consequences in the context of hepatocellular carcinoma.

The RNA profile of HP1-depleted cells recapitulated the effects observed upon depletion of nuclear RNA exosome components. PROMPTs and eRNAs were stabilized both in our HP1-deficient cells and in cells lacking core exosome (EXOSC3), NEXT (ZCCHC8), or PAXT (ZFC3H1) subunits, as reported in previous studies [50] [33]. In addition, ChIP-seq analysis revealed a dramatic reduction in the number of exosome-binding peaks across the genome in TKO cells, indicating a failure in local recruitment. This suggested that HP1 cooperated with NEXT and/or PAXT to promote exosome-mediated RNA decay by directing exosome components to specific chromatin loci. In this context, we noted that HP1 loss did not displace the RNA exosome from chromatin globally, nor did it affect RNA exosome subunit expression, supporting a direct role in targeting rather than chromatin association or complex stability.

The LTR-derived transcripts specifically detected in HP1 triple knockout (TKO) cells point to a dysregulation of RNA exosome activity. LTRs, derived from transposable elements (TEs), are typically embedded in heterochromatin and remain transcriptionally silent in most mammalian cells. This silencing is maintained through several mechanisms: DNA methylation predominates in somatic tissues and late embryonic stages, while in embryonic stem cells, H3K9me3-dependent pathways play a major role, particularly in repressing younger, more transcriptionally active retroelements [51]. Parallels can be drawn from other systems. In *S. pombe*, heterochromatic silencing involves two HP1 homologs: Chp2 represses transcription via the SHREC histone deacetylase complex, while Swi6 binds centromeric noncoding RNAs and promotes their degradation via the RNAi pathway or the RNA exosome [23,25]. In mESC, the human silencing hub (HUSH) complex contributes to TE silencing by being recruited to H3K9me3-marked chromatin through its MPP8 subunit. HUSH also cooperates with RNA degradation pathways, including the NEXT complex, to repress TEs [38,52]. Although we cannot fully exclude a loss of transcriptional repression in HP1-depleted BMEL cells, our data suggest that impaired RNA degradation is the dominant factor. Specifically, the LTR loci showing increased transcript accumulation in TKO cells did not overlap with HUSH-regulated loci identified by MPP8 ChIP-seq in mESCs (Supplementary Fig. 3C-D), making HUSH involvement in this context unlikely. However, other silencing factors, such as TNRC18—an H3K9me3 reader implicated in silencing of young ERV loci [53] — could still contribute. Overall, the increased LTR-derived RNA levels observed in TKO cells likely reflect a combined effect: the loss of HP1-mediated transcriptional repression and defective RNA degradation. This dual mechanism would resemble what has been described in yeast (SHREC and RNAi/exosome) and mESCs (HUSH and NEXT). This hypothesis awaits further investigation.

Although retroelements like LTRs have lost their ability to transpose in mammalian genomes, they still retain many transcriptional regulatory elements due to their viral origin. These elements can serve as platforms for transcription factor binding and initiation, thereby influencing various gene regulatory mechanisms [54]. Over time, many LTRs have been co-opted as alternative promoters, enhancers, or even chromatin insulators, such as at CTCF binding sites. In our previous work, we identified several examples of LTR exaptation as enhancers in BMEL cells [43], and we have also shown that increased transcription of ERVs in multiple sclerosis may reflect reactivation of embryonic enhancers of retroviral origin [55]. In the current study, we found that a relatively small subset of LTR elements gave rise to stabilized transcripts in HP1-deficient (TKO) cells. This suggests that HP1 proteins do not broadly repress LTRs, but instead act on transcriptionally active LTRs, particularly those with enhancer potential, much like the RNAi machinery, which targets loci based on RNA production. In our data, RNAs accumulating from enhancers and transcriptionally active LTRs were associated with increased transcription of nearby genes. While it remains debated whether eRNAs act through their transcription or as functional RNA molecules, they have been proposed to promote chromatin accessibility and modulate the recruitment of transcription factors and elongation regulators [56]. Their accumulation in HP1-depleted cells may thus contribute to the observed increase in RNAPII recruitment/phosphorylation, possibly by sequestering the negative elongation factor NELF and promoting the activation of P-TEFb [57].

Interestingly, genes involved in collagen and extracellular matrix formation were particularly sensitive to reduced RNA exosome activity. Both HP1 depletion and impaired exosome function were associated with their upregulation, and these genes also showed increased activity in HCC patients with low HP1 expression. The basis for this specificity remains unclear, but certain eRNAs and long noncoding RNAs (lncRNAs) are especially prone to exosome-mediated degradation and accumulate when the exosome is inactivated [58]. It is possible that enhancers regulating extracellular matrix genes belong to this susceptible class. From a disease perspective, overexpression of both HP1 and EXOSC components has been associated with poor prognosis in cancers such as HCC (Supplementary Fig. 6B and ref. [59]). Paradoxically, complete HP1 loss promotes liver tumorigenesis in aged mice [44]. We hypothesize that HP1 depletion leads to RNA accumulation, triggering antiviral immune responses. While this response may offer short-term protection and reduce initial tumor severity, its chronic activation could promote inflammation and tumor progression over time, particularly in the aging liver.

Methods

Cell lines

Het and TKO cells (Het 1, Het 3.2, Het 3.5, TKO1, TKO2, TKO3), as described in Figure 1A, were independent clones of BMEL cells derived from mouse embryonic liver, generated as previously described [44]. The cells were cultured in RPMI 1640 medium (Invitrogen) supplemented with 10% fetal bovine serum (FBS), 1% penicillin-streptomycin, 10 µg/mL insulin, 30 ng/mL IGF-II, and 50 ng/mL EGF, at 37 °C under 5% CO2.

Cell fractionation and total cell extracts

Cells (approximately 10^6 from a confluent 100 mm plate) were washed twice with ice-cold PBS directly on the plate then incubated on ice for 8 minutes in 10 mL of swelling buffer (SW): 10 mM Tris-HCl pH7.5, 2 mM MgCl2, 3 mM CaCl2, supplemented before use with 1x antiprotease (Roche), 0.5mM Na3VO4, 20mM beta-Glycerophosphate, 0.1mM DTT, 1U/ul RNasin (Promega). Cells were removed from the plate by scraping, and pelleted by centrifugation at 1600 rpm for 5 minutes at 4°C. Cell pellets were resuspended in 400 µL of lysis buffer (SW buffer containing 10% glycerol and 0.1% NP-40) and gently pipetted up and down 15 times using a P1000 tip and centrifuged at 2500 rpm for 5 minutes at 4°C to pellet the nuclei. The supernatant was considered as the cytosolic fraction. Nuclear pellets were resuspended in 400 µL of RB buffer containing 9 mM EDTA, 0.2 mM EGTA, 0.1% Triton X-100, supplemented before use with 1x antiprotease (Roche), 0.5mM Na3VO4, 20mM beta-Glycerophosphate, 1mM DTT, 1U/ul RNAsin (Promega) incubated for 15 minutes while rotating at 4°C, and centrifuged at 3000g for 5 minutes to pellet chromatin. The supernatant was considered as the nucleosolic fraction. Chromatin pellet were resuspended in 400 µL of RB buffer supplemented with 1% SDS and solubilized by sonication using a water bath sonicator (Diagenode) at high amplitude (6 cycles of 20 seconds). In parallel, total cell extracts were prepared in RIPA buffer: 150 mM NaCl, 50 mM Tris pH 8, 0.25% sodium deoxycholate, 0.1% SDS, 1% NP-40, freshly supplemented with 0.5 mM DTT and 1× protease inhibitor, RNAsin then incubated for 10 minutes on ice.

Co-immunoprecipitation assays

Approximately 10^6 cells from a confluent 100 mm plate were used to prepare nuclei according to the cell fractionation protocol described above. Nuclear pellets were resuspended in 0.5 ml of RIP buffer: 25mM TRIS pH 7.4, 150mM KCl, 2.5% glycerol, 0.3% NP-40 freshly supplemented with 1x antiprotease, 0.5 mM Na3VO4, 20mM beta-glycerophosphate, 0.1 mM DTT, 1U/ul RNAsin, and treated with 7U/mL TURBO DNase. The suspension was incubated at 37°C for 5 minutes. Samples were sheared by three cycles of sonication (10 seconds ON, 10 seconds OFF) using a Bioruptor (Diagenode), followed by a second incubation at 37°C for 5 minutes. The reaction was stopped by addition of 10 µl /mL of 0.5M EDTA per 0.5 ml. Samples were then centrifuged at 12000g for 10 minutes at 4°C. The resulting supernatant, referred to as "RIP extract", was used for subsequent immunoprecipitation (IP) experiments, and a portion of the RIP extract was reserved as input samples.

For each IP, 150 µl of RIP extract was combined with 3 µg of antibodies and 350 µl of RIP buffer. The mixture was incubated for 1h30 at 4°C on a rotating wheel. Saturated magnetic beads (Dynabeads M-280 sheep anti-rabbit IgG or Dynabeads Protein G, Invitrogen) were prepared by blocking 80 µl of beads per IP in PBS supplemented with 0.1% BSA, 0.5% NP40, and 0.1% polyvinylpyrrolidone (PVP) for 30 min at 4°C, followed by two washes with Wash V buffer: 0.1%

488 NP-40, 150mM NaCl, 20 mM TRIS.Cl pH8, 1mM EDTA. The saturated beads were resuspended
489 in 300 µl of Wash V buffer per IP, and added to the IP mixture. After 45 minutes of incubation,
490 beads were then washed twice with RIP buffer, twice with Wash V buffer, and once with TE/NP40
491 buffer: 10 mM TRIS pH7.4, 1 mM EDTA, 0.01 % NP-40. Beads were eluted in Laemmli sample
492 buffer. Both eluates and input samples were further processed for Western blot analysis.
493
494 **Cell fractionation for RNA preparation and sequencing (RNAseq)**
495 For total RNA extraction, cells were trypsinized, and the resulting pellet was washed with
496 PBS, and pelleted by centrifugation at 1800 rpm for 4 minutes at 4°C. The cell pellet was
497 resuspended in 1600 µL of Buffer D: 4 M guanidinium thiocyanate, 25 mM sodium citrate, pH
498 7.0, 0.5% (wt/vol) N-laurosylsarcosine and 0.1 M 2-mercaptoethanol [60], homogenized thoroughly
499 for total cell extracts, from which the total RNA was extracted.
500 For chromatin-associated and cytosolic RNA extraction, cells were resuspended, as
501 described above for cell fractionation, in 125 µL of ice-cold SW buffer and incubated on ice for 8
502 minutes. After swelling, 125 µL of lysis buffer was added, and the suspension was gently pipetted
503 15 times before centrifugation at 3500 rpm for 4 minutes at 4°C. The nuclei pellet was resuspended
504 in 250 µL of Buffer RB and incubated on ice for 15 minutes, followed by centrifugation at 6000
505 rpm for 4 minutes at 4°C, separating the chromatin and nucleosol. Both the nucleosol and
506 chromatin fractions were homogenized in Buffer D for RNA extraction.
507
508 RNA was extracted by addition to all fractions of 250 mM sodium acetate, 1 volume of
509 acidic phenol, and 0.2 volumes of chloroform. The samples were incubated on ice for 10 minutes,
510 followed by centrifugation at 14,000 g for 20 minutes at 4°C. The supernatant was collected and
511 mixed with an equal volume of chloroform, then centrifuged at 14,000 g for 5 minutes at 4°C. The
512 resulting supernatant was combined with an equal volume of isopropanol, vortexed thoroughly,
513 and incubated overnight at -20°C for RNA precipitation. The samples were centrifuged at 14,000
514 g for 20 minutes at 4°C, and the resulting pellet was washed with 75% ethanol, and resuspended
515 in 100 µL of Buffer D (diluted 1:10), supplemented with 0.5% Triton X-100, 0.4 M NaCl, and 1
516 µL of proteinase K. The mixture was incubated at 50°C with shaking at 850 rpm for 3 hours.
517 Subsequently, 250 mM sodium acetate, 300 µL of Buffer D, and 400 µL of acidic
518 phenol/chloroform were added to each fraction. The samples were centrifuged at 14,000 g for 15
519 minutes at 4°C, and the supernatant was collected. An equal volume of chloroform was added to
520 the supernatant, followed by centrifugation at 14,000 g for 20 minutes at 4°C. The final supernatant
521 was supplemented with Glycogen (2 µg/mL) as carrier and 1 volume of isopropanol, and the
522 samples were precipitated overnight at -20°C. The pellet was then washed with 75% ethanol and
523 resuspended in 50 µL of RNase-free water. The samples were incubated at 45°C with shaking at
524 800 rpm for 10 minutes. 40 µL was subjected to DNase treatment for 50 minutes at 37°C. RNA
525 integrity was verified by agarose gel electrophoresis. On all RNA fractions, total RNA library
526 preparation and sequencing were performed by Novogene (UK) Co., Ltd as part of their lncRNA-
527 seq service, which included directional library preparation with rRNA removal and sequencing on
528 the Illumina NovaSeq platform using paired-end 150 bp (PE150) reads.
529
530 **Chromatin immunopreciptation and sequencing (ChIPseq)**
531 BMEL cells were crosslinked following a modification of the protocol described in ref. [61].
532 Briefly cells were incubated in freshly prepared 2 mM DSG (Merck) in PBS for 50 minutes at
533 room temperature with occasional shaking. After three washes in PBS, cells were incubated for 10

534 minutes in 1% formaldehyde (Merck) in PBS. The crosslinking reaction was quenched with 125
535 mM glycine for 5 minutes at room temperature. Cells were washed with PBS, harvested, and
536 pelleted by centrifugation at 3000 g for 3 minutes. Cells were subsequently resuspended in 1.4
537 mL of freshly prepared swelling buffer (25mM Hepes pH 7.95, 10mM KCl, 10mM EDTA)
538 supplemented with protease inhibitors (Roche) and 0.5% NP-40. The suspension was incubated
539 on ice for 30 minutes, then pipetted up and down 50 times using a P1000 pipette tip. The cells
540 were centrifuged at 6000g for 2 minutes and resuspended in 300 µL of TSE150 buffer with 0.3 %
541 SDS (0.3% SDS, 1% Triton, 2mM EDTA, 20mM Tris-HCl pH8, 150mM NaCl) freshly
542 supplemented with protease inhibitors. Chromatin was sonicated in 1.5 mL tubes for a total of 15
543 minutes using cycles of 30 seconds ON and 30 seconds OFF, with the samples maintained in ice-
544 cold water. Following sonication, the samples were centrifuged at 14,000g for 30 minutes at 18°C.
545 An aliquot of supernatant was used to quantify chromatin and check DNA fragment size (typically
546 around 300 bp).
547 Chromatin immunoprecipitation (ChIP) was performed using 70 µg of chromatin and 4 µg
548 of the following antibodies : anti-MTR4/SKIV2L2 (Bethyl A300-615A), anti-ZC3H18 (Atlas
549 HPA 040847), anti-EXOSC10 (Bethyl A303-987A), anti-CTCF (Diagenode A2354-0023P), anti-
550 P-RNAPII (a mix of antibodies against phospho-Ser5 and phospho-Ser2, Abcam Ab5095 and
551 Ab5408, respectively), and anti-murine IgG (Merck). Immunoprecipitation was carried out
552 overnight on a rotating wheel at 4°C. Subsequently, 90 µL of Protein G beads (Dynabeads,
553 Invitrogen), blocked overnight at 4°C in blocking buffer containing 5% Buffer C (0.5% SDS, 10
554 mM Tris-Cl pH 8, 1 mM EDTA, 0.5 mM EGTA), 20% Buffer D 1.2× (1.2% Triton, 0.12% NaDoc,
555 180 mM NaCl, 12 mM Tris-Cl pH 8, 1.2 mM EDTA, 0.6 mM EGTA), 72% Wash Buffer V, 1.5%
556 BSA (Merck), and 1.5% Polyvinylpyrrolidone (Merck), were added to the IP samples and
557 incubated for 1h on a rotating wheel at 4°C. Ten percent of the chromatin was set aside as input.
558 Following immunoprecipitation, the beads were pelleted and subjected to sequential washes, each
559 performed for 3 minutes on a rotating wheel at room temperature using 1 mL of the following
560 buffers: Three washes in TSE150 buffer with 0.1 % SDS (0.1% SDS, 1% Triton, 2mM EDTA,
561 20mM Tris-HCl pH8, 150mM NaCl), then one wash in TSE500 buffer (TSE150 buffer with 0.1%
562 SDS and 500 mM NaCl), then one wash in buffer (10 mM Tris-HCl pH 8, 0.25 M LiCl, 0.5% NP-
563 40, 0.5% sodium deoxycholate, 1 mM EDTA), then two washes in TE buffer (10 mM Tris-HCl
564 pH 8, 1 mM EDTA). Elution was performed in 300 µL of elution buffer (1% SDS, 10 mM EDTA,
565 50 mM Tris-HCl pH 8) by vortexing vigorously, followed by incubation at 65°C for 15 minutes.
566 A second elution was performed using 100 µL of elution buffer. Both eluates were collected, and
567 the beads were rinsed in 100 µL of TE buffer with 1% SDS, subsequently added to the pool of
568 eluates. Both the immunoprecipitated and input chromatin samples were incubated overnight at
569 65°C to reverse crosslink, followed by proteinase K and RNase A treatments. DNA was isolated
570 using a NucleoSpin PCR purification kit (Macherey Nagel), and concentrations were measured
571 using a Qubit fluorometer (Invitrogen). Purified ChIP samples were processed for Illumina paired-
572 end (PE40) sequencing performed at the Genom'IC core facility (Paris, France).
573
574 **Western Blotting analysis**
575 Protein samples were denatured by the addition of Laemmli sample buffer (Bio-Rad) with
576 reducing agent at 100°C for 10 minutes and separated by SDS-PAGE (Bio-Rad, Criterion XT),
577 then transferred to a nitrocellulose membrane. Transferred proteins were visualized by Ponceau S
578 staining, and the membranes were incubated overnight at 4°C in PBS-T (PBS, 0.1% Tween 20),
579 containing 5% (w/v) non-fat dry milk. The membranes were then incubated for 1h30 at room

temperature with primary antibodies at the appropriate dilution in PBS-T (as described in the Western blot antibodies section). After three 5-minute washes in PBS-T, the membranes were incubated for 1h30 with secondary antibodies (Starbright Blue 700 anti-rabbit/mouse IgG (Biorad), or rabbit true blot (Rockland), all diluted 1/4000), followed by three additional 5-minute washes. Protein detection was performed either by fluorescence at 700 nm or by chemiluminescence using the Pierce™ ECL Plus Western Blotting Substrate (Thermo Fisher Scientific) and visualized with a ChemiDoc MP imaging system (Bio-Rad).

Western blot antibodies

Antibodies	Dilution	References
Anti-EXOSC3	1/1000	Proteintech 15062-I-AP
Anti-EXOSC9	1 /1000	Abcam ab156686
Anti-EXOSC10	1/1000	Bethyl A303-987A
Anti-MTR4/SKIV2L2	1 /1000	Bethyl A300-615A
Anti-ZC3H18	1 /2000	Bethyl A304-682A
Anti-CTCF	1/1000	Diagenode A2354-0023P
Anti-HP1α	1 /1000	Euromedex 2G9
Anti-HP1β	1/2000	Euromedex 1A9
Anti-HP1γ	1/3000	Euromedex 1G6
Anti-H3K9me3	1/2000	Abcam ab8898

ATACseq

Chromatin accessibility assays were performed on each of the six Het and TKO BMEL clones according to the protocol described in ref. [62], with an ATACseq kit (ActiveMotif, 53150). Paired-end (PE40) sequencing of the dual-index ATACseq libraries was performed by Novogene (UK) Co., Ltd.

CUT&Tag

CUT&Tag assays were performed on two independent biological replicates of Het and TKO BMEL cells according to the protocol by [63], but with the NE1 buffer (https://www.protocols.io/view/bench-top-cut-amp-tag-kqdg34qdpl25/v3) to permeabilize cells, and with the same anti-HP1α, -HP1β, -HP1γ, -H3K9me3 as used in Western blot analyses, and with anti-H3K27me3 (Cell Signaling Technol. 9733). Libraries were obtained with 15-16 PCR amplification cycles such that at least a faint ladder of nucleosome-sized bands were visible using an Agilent Tape Station High-Sensitivity D1000 Screen Tape representing DNA concentrations of at least 200 pg/µl for anti-HP1 CUT&Tag reactions with Het cells, and at least 10-fold lower concentrations for the same reactions using TKO cells. 40 nt paired-end sequencing was performed at the I2BC sequencing platform. Reads were aligned on the mm10 reference genome with bowtie2 (parameters: --end-to-end --very-sensitive --no-mixed --no-discordant -k 1 -X 1000 --phred33 -I 25 -p 24 -x mm10). Bigwig files were generated from two merged HP1 CUT&Tag replicates, and they were normalized using CPM.

Bioinformatics analyses

RNAseq data analysis : Mapping was carried out with STAR (v2.6.0b) (parameters: –outFilterMismatchNmax 1 – outSAMmultNmax 1 –outMultimapperOrder Random –

outFilterMultimapNmax 30). The reference genome was GRCm38 Mus musculus primary assembly from Ensembl. The SAM files were converted to BAM files and sorted by coordinate using samtools (v1.8). Gene expression analysis was performed with the DESeq2 (v1.18.1) package. P-values from the differential gene expression test were adjusted for multiple testing according to the Benjamini and Hochberg procedure.

ChIPseq data analysis : Raw ChIP-seq data in Fastq format were subjected to quality control using FastQC (v0.11.9). ChIP-seq reads were mapped to mm10 using bowtie2 (v2.3.4) (parameters: -N 0 -k 1 –very-sensitive-local). We then selected reads with a MAPQ equal or higher than 30 corresponding to uniquely mapped reads for further analysis. Peak calling was performed using MACS2 (v.2.1.1) (parameters: -p 0.05).

ATACseq data analysis : For chromatin accessibility profiling, Bowtie2 was used with the parameters --very-sensitive -X 2000 to accommodate the broad range of ATAC-seq fragment sizes, and --maxins 500 --no-discordant --no-mixed -k 1 to eliminate multi-mapping reads. Aligned BAM files were sorted and indexed using SAMtools (v1.8). ATAC-seq peaks were called using MACS2 (v2.2.9.1) with the parameters --nomodel, --shift -100, and --extsize 200, which are recommended for ATAC-seq to account for the Tn5 transposase cutting pattern. Peaks were identified using a q-value threshold of 0.01 (-q 0.01), and signal tracks were generated in bedGraph format with -B --SPMR. The genome size was set to mouse (-g mm), and input files were sorted BAM files in BAM format (-f BAM).

For all high throughput experiments, Bigwig files were generated from BAM files with bamCoverage (parameter: –normalizeUsing CPM) from Deeptools (v3.1.3)

Pathway analyses with gene names were performed with Enrichr (https://maayanlab.cloud/Enrichr/). The FDR (adjusted p-value, denoted p-adj in Figures) of each path entry served as the significance threshold.

Definition of genomic regions and categories

LTR, SINE, LINE, and MMSAT regions were defined by the RepClass field in the Repeat masker database in the UCSC table browser (https://genome.ucsc.edu/). The enhD Distal enhancers were defined as the dELS/enhD category in the Encyclopedia of DNA Elements (ENCODE) candidate cis-regulatory element (cCRE) database in the UCSC table browser. Extragenic repeats and enhD elements were defined relative to genes in the Ensembl Grc38 database (https://www.ensembl.org/). Promoter associated transcripts (PROMPT) regions were defined as 2kb upstream of transcription start sites (TSS) of genes. Exons were defined according to the Ensembl GRCm38 database. The list of 23808 Genes was defined according to the Ensembl Grc38 database, after removing all the entries with names beginning with "Mir", "Rik", and "Gm", for the sake of clarity of the average density profiles.

The EnhD (Up, Down, Unchanged, and Closed) categories were created according to their activity as defined by ATACseq read counts obtained by featurecounts on distal enhancer elements (enhD) in ENCODE database. EnhD categories are as follows :

enhD Up (ATACseq reads>10 p-val.<0.05 FC TKO vs. Het >=4),

enhD Down (ATACseq reads >10, p-val.<0.05 FC TKO vs. Het <= 0.25),

enhD Unchanged (ATACseq reads >10, 0.9<FC<1.1),

enhD Closed (ATACseq reads <2).

RNA Read counts on genomic regions

Quantification of uniquely mapped reads from the transcriptome was carried out with featureCounts (v1.6.1) from the Subread suite [64], with the following parameters: -p -B -C -s 1 --minOverlap 25. FeatureCounts with these parameters counted only uniquely mapped reads with both paired-ends aligned (-p -B).

Chromatin and cytoplasmic stranded RNA reads were counted on extragenic repeats only in order to evaluate self-expressed repeats and avoid counting reads on gene-embedded repeats which would reflect expression of the surrounding gene and not the repeat itself. Read counts were the results of stranded reads counted in regions substracted by stranded reads counted in the 200nt region upstream of repeats adjusted for their size.

Transcriptome reads on PROMPT were counted antisense, corresponding to upstream-antisense RNA (uaRNA), relative to the orientation of their adjacent gene substracted by antisense read counts in its first exon adjusted for their respective size. Transcriptome read counts on enhD were substracted by read counts in the highest of the two adjacent 200nt region upstream or downstream of each enhD adjusted for their respective size. All genomic regions counted for RNA levels were considered expressed when two or more reads (or ten or more reads on exons) were counted in average of the triplicate samples, in either Het or TKO or both, after substracting reads from size-normalized adjacent regions (illustrated in Fig. 2B and 2E). In order to avoid excluding the elements expressed only in Het or in TKO, a pseudo-count of 0.1 was added to the mean RNA read counts before transformation into Log2 (illustrated in Fig. 2C, 2D, 2F and 2G).

Data visualization

BigWig files of samples or merged replicates were visualized with the Integrative Genomics Viewer (IGV version 2.8.10). Heatmaps and profiles were generated with the computeMatrix, plotProfile and plotHeatmap tools of the Deeptools package (v3.1.3). The patient survival curves in Supplementary Fig. 6B are based upon data generated by the TCGA Research Network: https://www.cancer.gov/tcga, obtained from the Human Protein Atlas database (proteinatlas.org).

Statistical analyses

The statistical tests performed are described in Fig. legends or in the Methods section. Significance level was evaluated by two-tailed Student's t-test as indicated in Fig. legends. The exact (n) number of samples is indicated in each figure. No statistical method was used to predetermine sample size. No data were excluded from the analyses.

Data availability

All RNA-seq, ChIP-seq, ATAC-seq, and CUT&Tag datasets generated during this study are available in the EBI BioStudies database (http://www.ebi.ac.uk/biostudies) under accession numbers: E-MTAB-15194, E-MTAB-15196, E-MTAB-15197, and E-MTAB-15189, respectively.

Acknowledgments

The authors wish to thank Enzo Becherel for its technical help. This work has been supported by PhD fellowships from La Ligue Nationale Contre le Cancer (to HS) and by grants from Aviesan ITMO Cancer (Plan Cancer, AAP ARN non-codants) and Institut National du Cancer (INCa,

PLBIO-2020-107). We acknowledge the sequencing and bioinformatics expertise of the I2BC High-throughput sequencing facility, supported by France Génomique (funded by the French National Program "Investissement d'Avenir" ANR-10-INBS-09).

Author Contributions

Experimental investigation: H.S., L.S., K.G., E.B., F.C., C.Ma., C.R.
Bioinformatic analysis: H.S., M.C., C.Ma., C.Mu., C.R.
Funding acquisition: C.Mu.
Writing original draft: H.S., C.Mu., C.R.
Manuscript review and editing: F.C., C.Ma., C.Mu., C.R.
All authors read and approved the final version of the manuscript.

Competing Interests

The authors declare no competing interests.

Material availability

The Het and TKO BMEL cell lines are readily available from the authors upon request.

References

1. Grewal, S.I.S. The molecular basis of heterochromatin assembly and epigenetic inheritance. *Mol Cell* **83**, 1767-1785 (2023).
2. Bannister, A.J. et al. Selective recognition of methylated lysine 9 on histone H3 by the HP1 chromo domain. *Nature* **410**, 120-4 (2001).
3. Jacobs, S.A. et al. Specificity of the HP1 chromo domain for the methylated N-terminus of histone H3. *EMBO J* **20**, 5232-41 (2001).
4. Lachner, M., O'Carroll, D., Rea, S., Mechtler, K. & Jenuwein, T. Methylation of histone H3 lysine 9 creates a binding site for HP1 proteins. *Nature* **410**, 116-20 (2001).
5. Lechner, M.S., Schultz, D.C., Negorev, D., Maul, G.G. & Rauscher, F.J., 3rd. The mammalian heterochromatin protein 1 binds diverse nuclear proteins through a common motif that targets the chromoshadow domain. *Biochem Biophys Res Commun* **331**, 929-37 (2005).
6. Thiru, A. et al. Structural basis of HP1/PXVXL motif peptide interactions and HP1 localisation to heterochromatin. *EMBO J* **23**, 489-99 (2004).
7. Hiragami-Hamada, K. & Fischle, W. RNAs - physical and functional modulators of chromatin reader proteins. *Biochim Biophys Acta* **1839**, 737-42 (2014).
8. Minc, E., Courvalin, J.C. & Buendia, B. HP1gamma associates with euchromatin and heterochromatin in mammalian nuclei and chromosomes. *Cytogenet Cell Genet* **90**, 279-84 (2000).
9. Piacentini, L. et al. Heterochromatin protein 1 (HP1a) positively regulates euchromatic gene expression through RNA transcript association and interaction with hnRNPs in Drosophila. *PLoS Genet* **5**, e1000670 (2009).
10. Vakoc, C.R., Mandat, S.A., Olenchock, B.A. & Blobel, G.A. Histone H3 lysine 9 methylation and HP1gamma are associated with transcription elongation through mammalian chromatin. *Mol Cell* **19**, 381-91 (2005).
11. Allo, M. et al. Control of alternative splicing through siRNA-mediated transcriptional gene silencing. *Nat Struct Mol Biol* **16**, 717-24 (2009).
12. Ameyar-Zazoua, M. et al. Argonaute proteins couple chromatin silencing to alternative splicing. *Nat Struct Mol Biol* **19**, 998-1004 (2012).
13. Saint-Andre, V., Batsche, E., Rachez, C. & Muchardt, C. Histone H3 lysine 9 trimethylation and HP1gamma favor inclusion of alternative exons. *Nat Struct Mol Biol* **18**, 337-44 (2011).
14. Smallwood, A. et al. CBX3 regulates efficient RNA processing genome-wide. *Genome Res* **22**, 1426-36 (2012).
15. Yearim, A. et al. HP1 is involved in regulating the global impact of DNA methylation on alternative splicing. *Cell Rep* **10**, 1122-34 (2015).
16. Porozhan, Y. et al. Defective Integrator activity shapes the transcriptome of patients with multiple sclerosis. *Life Sci Alliance* **7**(2024).
17. Skourti-Stathaki, K., Kamieniarz-Gdula, K. & Proudfoot, N.J. R-loops induce repressive chromatin marks over mammalian gene terminators. *Nature* **516**, 436-9 (2014).
18. Maison, C. et al. Higher-order structure in pericentric heterochromatin involves a distinct pattern of histone modification and an RNA component. *Nat Genet* **30**, 329-34 (2002).
19. Muchardt, C. et al. Coordinated methyl and RNA binding is required for heterochromatin localization of mammalian HP1alpha. *EMBO Rep* **3**, 975-81 (2002).

786 20. Maison, C. et al. SUMOylation promotes de novo targeting of HP1alpha to pericentric
787 heterochromatin. *Nat Genet* **43**, 220-7 (2011).
788 21. Mata-Garrido, J. et al. The Heterochromatin protein 1 is a regulator in RNA splicing
789 precision deficient in ulcerative colitis. *Nat Commun* **13**, 6834 (2022).
790 22. Rachez, C. et al. HP1gamma binding pre-mRNA intronic repeats modulates RNA
791 splicing decisions. *EMBO Rep* **22**, e52320 (2021).
792 23. Motamedi, M.R. et al. HP1 proteins form distinct complexes and mediate
793 heterochromatic gene silencing by nonoverlapping mechanisms. *Mol Cell* **32**, 778-90
794 (2008).
795 24. Buhler, M., Haas, W., Gygi, S.P. & Moazed, D. RNAi-dependent and -independent RNA
796 turnover mechanisms contribute to heterochromatic gene silencing. *Cell* **129**, 707-21
797 (2007).
798 25. Keller, C. et al. HP1(Swi6) mediates the recognition and destruction of heterochromatic
799 RNA transcripts. *Mol Cell* **47**, 215-27 (2012).
800 26. Kilchert, C., Wittmann, S. & Vasiljeva, L. The regulation and functions of the nuclear
801 RNA exosome complex. *Nat Rev Mol Cell Biol* **17**, 227-39 (2016).
802 27. Tomecki, R., Drazkowska, K., Kobylecki, K. & Tudek, A. SKI complex: A multifaceted
803 cytoplasmic RNA exosome cofactor in mRNA metabolism with links to disease,
804 developmental processes, and antiviral responses. *Wiley Interdiscip Rev RNA* **14**, e1795
805 (2023).
806 28. Rambout, X. & Maquat, L.E. Nuclear mRNA decay: regulatory networks that control
807 gene expression. *Nat Rev Genet* **25**, 679-697 (2024).
808 29. LaCava, J. et al. RNA degradation by the exosome is promoted by a nuclear
809 polyadenylation complex. *Cell* **121**, 713-24 (2005).
810 30. Andersson, R. et al. An atlas of active enhancers across human cell types and tissues.
811 *Nature* **507**, 455-461 (2014).
812 31. Lubas, M. et al. Interaction profiling identifies the human nuclear exosome targeting
813 complex. *Mol Cell* **43**, 624-37 (2011).
814 32. Preker, P. et al. RNA exosome depletion reveals transcription upstream of active human
815 promoters. *Science* **322**, 1851-4 (2008).
816 33. Meola, N. et al. Identification of a Nuclear Exosome Decay Pathway for Processed
817 Transcripts. *Mol Cell* **64**, 520-533 (2016).
818 34. Weick, E.M. & Lima, C.D. RNA helicases are hubs that orchestrate exosome-dependent
819 3'-5' decay. *Curr Opin Struct Biol* **67**, 86-94 (2021).
820 35. Andersen, P.R. et al. The human cap-binding complex is functionally connected to the
821 nuclear RNA exosome. *Nat Struct Mol Biol* **20**, 1367-76 (2013).
822 36. Phillips, J.E. & Corces, V.G. CTCF: master weaver of the genome. *Cell* **137**, 1194-211
823 (2009).
824 37. Laffleur, B. et al. Noncoding RNA processing by DIS3 regulates chromosomal
825 architecture and somatic hypermutation in B cells. *Nat Genet* **53**, 230-242 (2021).
826 38. Garland, W. et al. Chromatin modifier HUSH co-operates with RNA decay factor NEXT
827 to restrict transposable element expression. *Mol Cell* **82**, 1691-1707 e8 (2022).
828 39. Wu, Y. et al. Nuclear Exosome Targeting Complex Core Factor Zcchc8 Regulates the
829 Degradation of LINE1 RNA in Early Embryos and Embryonic Stem Cells. *Cell Rep* **29**,
830 2461-2472 e6 (2019).

831 40. Silla, T. et al. The human ZC3H3 and RBM26/27 proteins are critical for PAXT-
832 mediated nuclear RNA decay. *Nucleic Acids Res* **48**, 2518-2530 (2020).
833 41. Winczura, K. et al. Characterizing ZC3H18, a Multi-domain Protein at the Interface of
834 RNA Production and Destruction Decisions. *Cell Rep* **22**, 44-58 (2018).
835 42. Zaidan, N.Z. et al. Compartmentalization of HP1 Proteins in Pluripotency Acquisition
836 and Maintenance. *Stem Cell Reports* **10**, 627-641 (2018).
837 43. Calvet, S. et al. Endogenous Retroviral Sequences Behave as Putative Enhancers
838 Controlling Gene Expression through HP1-Regulated Long-Range Chromatin
839 Interactions. *Cells* **11**(2022).
840 44. Saksouk, N. et al. The mouse HP1 proteins are essential for preventing liver
841 tumorigenesis. *Oncogene* **39**, 2676-2691 (2020).
842 45. Hediger, F. & Gasser, S.M. Heterochromatin protein 1: don't judge the book by its cover!
843 *Curr Opin Genet Dev* **16**, 143-50 (2006).
844 46. Ostapcuk, V. et al. Activity-dependent neuroprotective protein recruits HP1 and CHD4 to
845 control lineage-specifying genes. *Nature* **557**, 739-743 (2018).
846 47. Candia, J. et al. The genomic landscape of Mongolian hepatocellular carcinoma. *Nat*
847 *Commun* **11**, 4383 (2020).
848 48. Mullani, N. et al. Reduced RNA turnover as a driver of cellular senescence. *Life Sci*
849 *Alliance* **4**(2021).
850 49. Roy, A.M., Iyer, R. & Chakraborty, S. The extracellular matrix in hepatocellular
851 carcinoma: Mechanisms and therapeutic vulnerability. *Cell Rep Med* **4**, 101170 (2023).
852 50. Lubas, M. et al. The human nuclear exosome targeting complex is loaded onto newly
853 synthesized RNA to direct early ribonucleolysis. *Cell Rep* **10**, 178-92 (2015).
854 51. Bulut-Karslioglu, A. et al. Suv39h-dependent H3K9me3 marks intact retrotransposons
855 and silences LINE elements in mouse embryonic stem cells. *Mol Cell* **55**, 277-90 (2014).
856 52. Matkovic, R. et al. TASOR epigenetic repressor cooperates with a CNOT1 RNA
857 degradation pathway to repress HIV. *Nat Commun* **13**, 66 (2022).
858 53. Zhao, S. et al. TNRC18 engages H3K9me3 to mediate silencing of endogenous
859 retrotransposons. *Nature* **623**, 633-642 (2023).
860 54. Fueyo, R., Judd, J., Feschotte, C. & Wysocka, J. Roles of transposable elements in the
861 regulation of mammalian transcription. *Nat Rev Mol Cell Biol* **23**, 481-497 (2022).
862 55. Azebi, S., Batsche, E., Michel, F., Kornobis, E. & Muchardt, C. Expression of
863 endogenous retroviruses reflects increased usage of atypical enhancers in T cells. *EMBO*
864 *J* **38**(2019).
865 56. Sartorelli, V. & Lauberth, S.M. Enhancer RNAs are an important regulatory layer of the
866 epigenome. *Nat Struct Mol Biol* **27**, 521-528 (2020).
867 57. Schaukowitch, K. et al. Enhancer RNA facilitates NELF release from immediate early
868 genes. *Mol Cell* **56**, 29-42 (2014).
869 58. Pefanis, E. et al. RNA exosome-regulated long non-coding RNA transcription controls
870 super-enhancer activity. *Cell* **161**, 774-89 (2015).
871 59. Zhang, Y., Yang, X., Hu, Y. & Huang, X. Integrated Bioinformatic Investigation of
872 EXOSCs in Hepatocellular Carcinoma Followed by the Preliminary Validation of
873 EXOSC5 in Cell Proliferation. *Int J Mol Sci* **23**(2022).
874 60. Chomczynski, P. & Sacchi, N. The single-step method of RNA isolation by acid
875 guanidinium thiocyanate-phenol-chloroform extraction: twenty-something years on. *Nat*
876 *Protoc* **1**, 581-5 (2006).

877 61. Festuccia, N. et al. Mitotic binding of Esrrb marks key regulatory regions of the
878 pluripotency network. *Nat Cell Biol* **18**, 1139-1148 (2016).
879 62. Buenrostro, J.D., Giresi, P.G., Zaba, L.C., Chang, H.Y. & Greenleaf, W.J. Transposition
880 of native chromatin for fast and sensitive epigenomic profiling of open chromatin, DNA-
881 binding proteins and nucleosome position. *Nat Methods* **10**, 1213-8 (2013).
882 63. Kaya-Okur, H.S. et al. CUT&Tag for efficient epigenomic profiling of small samples and
883 single cells. *Nat Commun* **10**, 1930 (2019).
884 64. Liao, Y., Smyth, G.K. & Shi, W. featureCounts: an efficient general purpose program for
885 assigning sequence reads to genomic features. *Bioinformatics* **30**, 923-30 (2014).
886

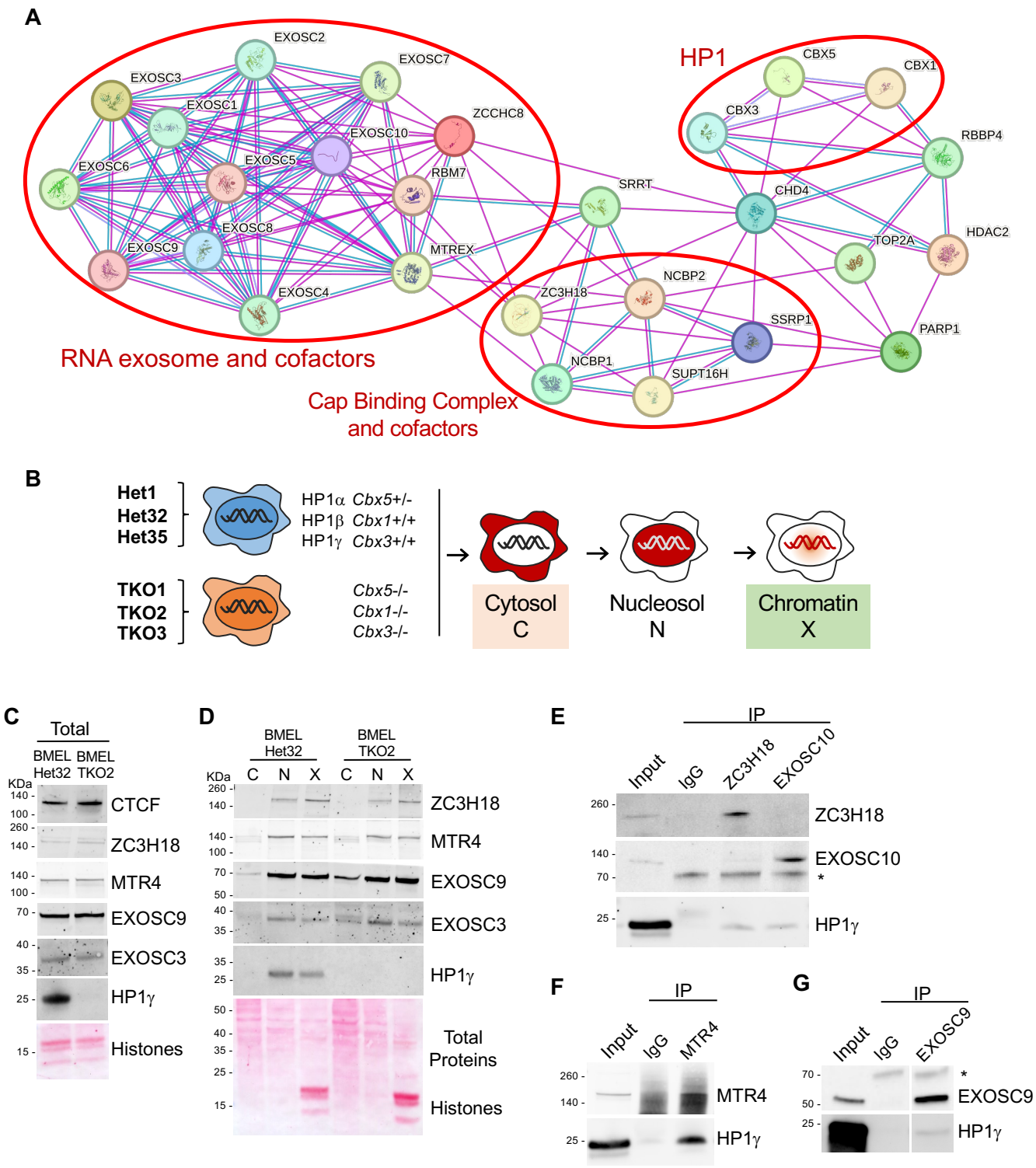

Fig. 1: Protein-protein association between HP1 and the RNA Exosome.
A. String analysis of known physical proteins associations among factors co-precipitating with ZC3H18 proteins, identified by interaction profiling of ZC3H18, in ref. [41]. Pink and blue network edges correspond to protein associations based on experiments or curated databases, respectively. **B.** Genotype and subcellular fractionation scheme of the six BMEL clones expressing (Het) or not (Triple Knock-out, TKO) HP1 proteins used in this study. **C.** Protein levels in total extracts, and **D,** subcellular distribution in the three fractions, cytosolic (C), nucleosoluble (N), and chromatin (X), depicted in Figure 1B of indicated exosome subunits and cofactors in Het and TKO cells by Western blot analysis and Ponceau staining of total proteins. **E, F, G.** Co-immunoprecipitation of HP1γ by MTR4, ZC3H18, EXOSC10, or EXOSC9 in BMEL nuclear extracts.

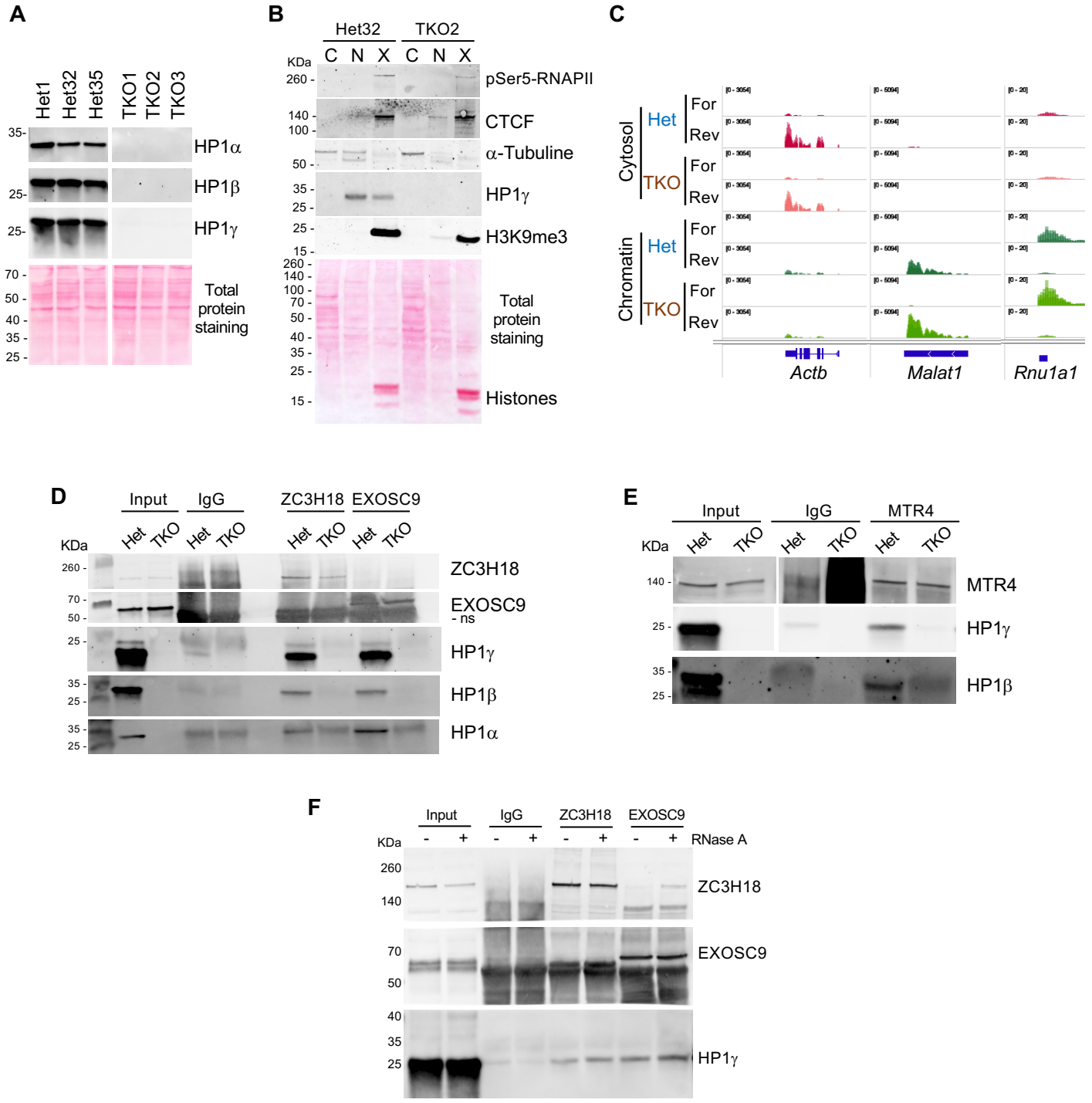

Supplementary Fig. 1: Cell fractionation and co-immunoprecipitation assays
A. Levels of HP1 proteins in all BMEL clones by Western blot analysis. **B.** Distribution of indicated proteins in the subcellular fractions (C, N, X, as in Fig. 1B) in two representative Het and TKO clones by Western blot analysis, and total proteins by Ponceau S staining. **C**. Genome views as in Figure 2A of the distribution of RNA density profiles between cytosolic and chromatin fractions for Actb mRNA and the nuclear Malat1 RNA or U-snRNA. Distribution reflects the expected subcellular localizations of the depicted RNA species. **D, E.** Co-immunoprecipitation assays of HP1a, HP1b, and HP1g by MTR4, ZC3H18, or EXOSC9, compared to IgG. **F.** RNA-independent co-immunoprecipitation of HP1g by ZC3H18 and EXOSC9. HP1g signal is not lost upon RNase A treatment.

Fig. 2

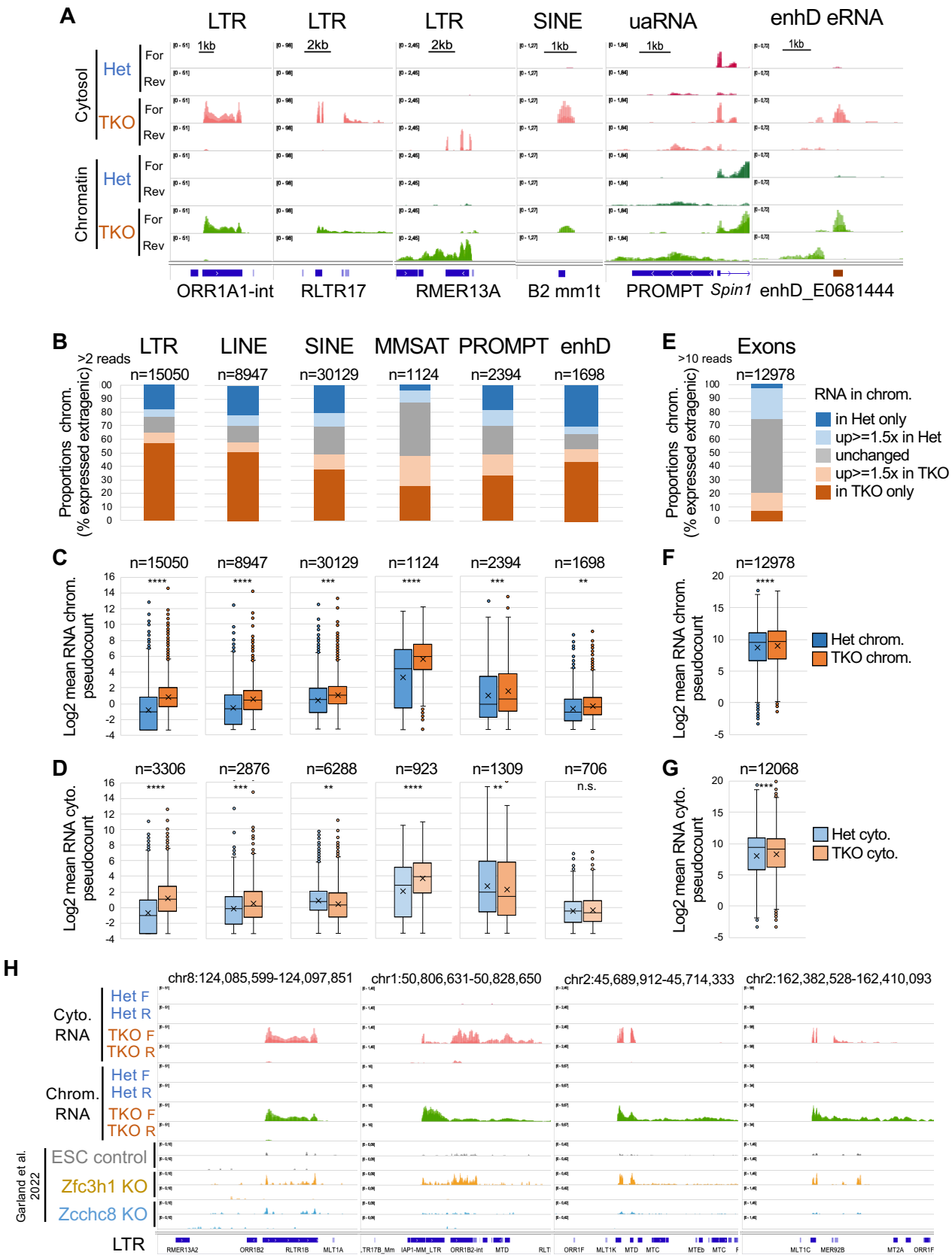
A
LTR
LTR
LTR
SINE
uaRNA
enhD eRNA
Cytosol
Chromatin
Het
TKO
For
Rev
1kb
2kb
ORR1A1-int
RLTR17
RMER13A
B2 mm1t
PROMPT
Spin1
enhD_E0681444
B
LTR
LINE
SINE
MMSAT
PROMPT
enhD
>2 reads
n=15050
n=8947
n=30129
n=1124
n=2394
n=1698
Proportions chrom. (% expressed extragenic)
E
Exons
>10 reads
n=12978
RNA in chrom.
in Het only
up>=1.5x in Het
unchanged
up>=1.5x in TKO
in TKO only
C
Log2 mean RNA chrom. pseudocount
F
Het chrom.
TKO chrom.
D
n=3306
n=2876
n=6288
n=923
n=1309
n=706
n.s.
Log2 mean RNA cyto. pseudocount
G
n=12068
Het cyto.
TKO cyto.
H
chr8:124,085,599-124,097,851
chr1:50,806,631-50,828,650
chr2:45,689,912-45,714,333
chr2:162,382,528-162,410,093
Cyto. RNA
Chrom. RNA
Garland et al. 2022
ESC control
Zfc3h1 KO
Zcchc8 KO
LTR

Fig. 2: Chromatin-enriched RNA is increased in TKO cells and stabilized in the cytoplasm.
A. Genome views of RNA density profiles (merged triplicates) in chromatin (green) and cytosolic (red) fractions, at indicated genomic loci showing TKO-specific or TKO-increased RNA. **B, C, D.** RNA levels by counting uniquely mapped reads on repeated elements (LTR, LINE, SINE, MMSAT4), Promoter upstream antisense RNA (PROMPT), distal enhancers (enhD) and exons of ensembl genes. **B.** Cumulative histograms of proportions of the indicated genomic regions expressing RNA (more than 2 reads) by comparison of the three Het clones with the three TKO clones. Five categories discriminate expression on chromatin in TKO only (brown), increased in TKO (salmon), in Het only (dark blue), increased in Het (light blue), unchanged (grey). **C, D.** Boxplots of mean RNA read counts in chromatin (C) or in the cytosol (D) on genomic regions as in B. in Het (blue) or TKO (orange). Asterisks represent significance level by unpaired two-tailed Student's t-test (**** $p < 0.0001$, *** $p < 0.001$, ** $p < 0.01$, * $p < 0.05$, n.s., not significant). **E, F, G.** Histogram and boxplots as in figures B, C, D, for proportions and counts on expressed exons (more than 10 reads). **H.** Transcriptome profiles in Het or TKO chromatin (green) or cytoplasm (red) compared with transcriptomes of mESC invalidated for the expression of NEXT or PAXT Exosome complex components, *Zcchc8* KO (sky blue profiles) or *Zfc3h1* KO (yellow profiles) and control mESC (grey profiles) (GSE178550; Garland et al., 2022). All boxplots in Fig 2 show median (central line), IQR (25th and 75th percentiles, box limits); whiskers extend to 1.5 x IQR.; points are values of outliers.

Fig. 3

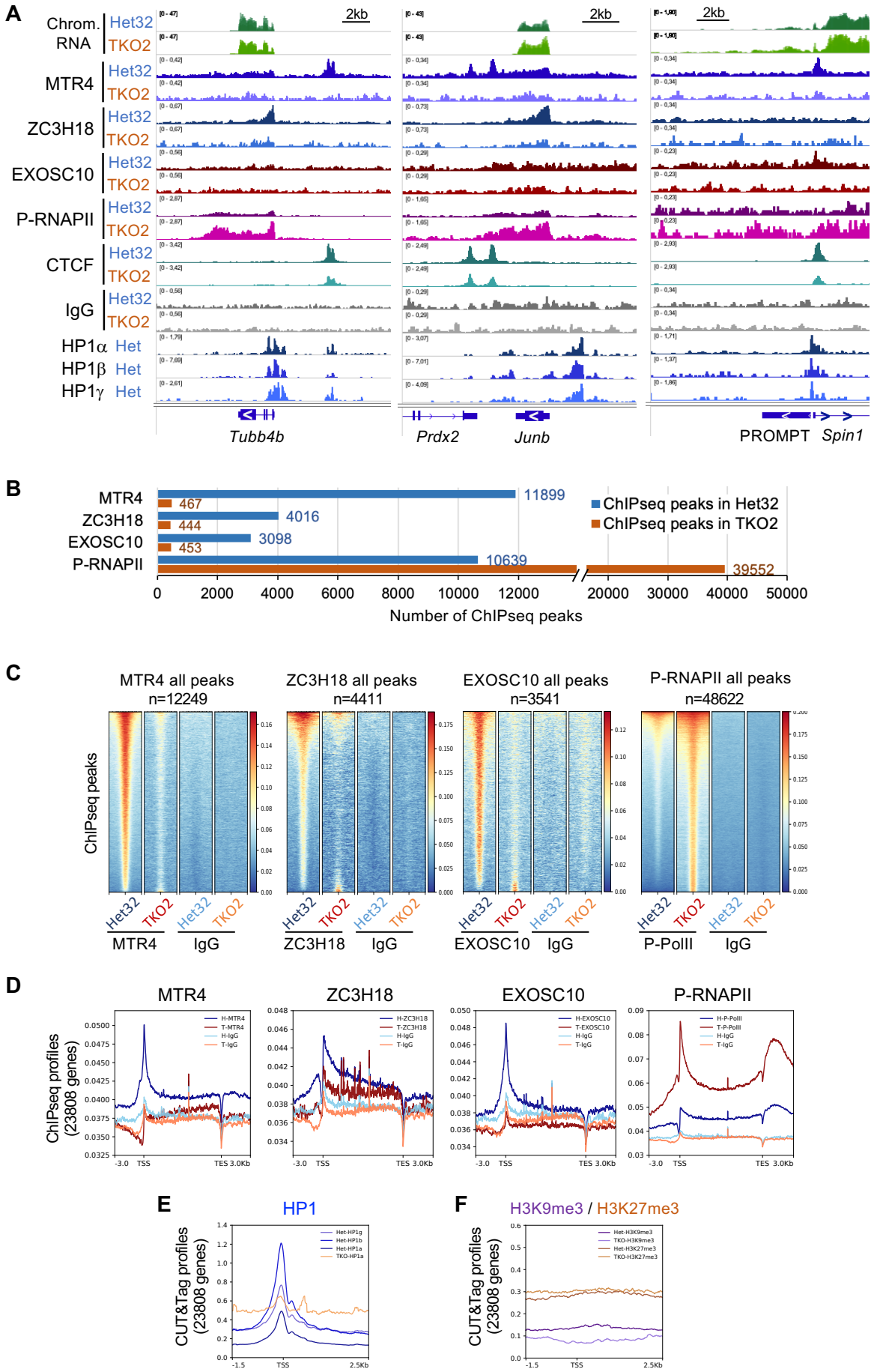
A
Chrom. RNA
Het32
TKO2
MTR4
ZC3H18
EXOSC10
P-RNAPII
CTCF
IgG
HP1α Het
HP1β Het
HP1γ Het
2kb
Tubb4b
Prdx2
Junb
PROMPT
Spin1
B
MTR4
ZC3H18
EXOSC10
P-RNAPII
467
11899
444
4016
453
3098
10639
39552
ChIPseq peaks in Het32
ChIPseq peaks in TKO2
Number of ChIPseq peaks
C
MTR4 all peaks
n=12249
ZC3H18 all peaks
n=4411
EXOSC10 all peaks
n=3541
P-RNAPII all peaks
n=48622
ChIPseq peaks
Het32
TKO2
MTR4
IgG
ZC3H18
EXOSC10
P-PolII
D
MTR4
ZC3H18
EXOSC10
P-RNAPII
ChIPseq profiles (23808 genes)
TSS
TES 3.0Kb
E
HP1
CUT&Tag profiles (23808 genes)
TSS
2.5Kb
F
H3K9me3 / H3K27me3
CUT&Tag profiles (23808 genes)
TSS
2.5Kb

Fig. 3: ChIPseq analysis reveals an HP1-dependent targeting of Nuclear RNA exosome and cofactors to chromatin loci.

A. Genome views of chromatin RNA density profiles (top), ChIPseq profiles of indicated proteins, and HP1 CUT&Tag density profiles (bottom) on indicated loci. **B.** Number of ChIPseq peaks versus IgG defined by MACS2 analysis for the indicated proteins in Het32 (blue) and TKO2 (brown). **C.** Heatmaps of genome-wide ChIPseq densities centered on ChIPseq peaks in both Het32 and TKO2 combined in a single list (all peaks). **D.** Metagene analysis of ChIPseq profiles of the indicated proteins on 23808 gene bodies defined as TSS to TES intervals, in Het32 (dark blue), in TKO2 (dark red), compared to IgG profiles in Het32 and TKO2 (salmon and light blue profiles, respectively). **E.** CUT&Tag profiles at gene TSS for the three HP1 proteins (E) in Het (blue profiles), and HP1a in TKO (salmon profile). **F.** Cut&Tag profiles at TSS for H3K9me3 (purple) and H3K27me3 (brown) histone marks in Het (dark colors) and in TKO (light colors).

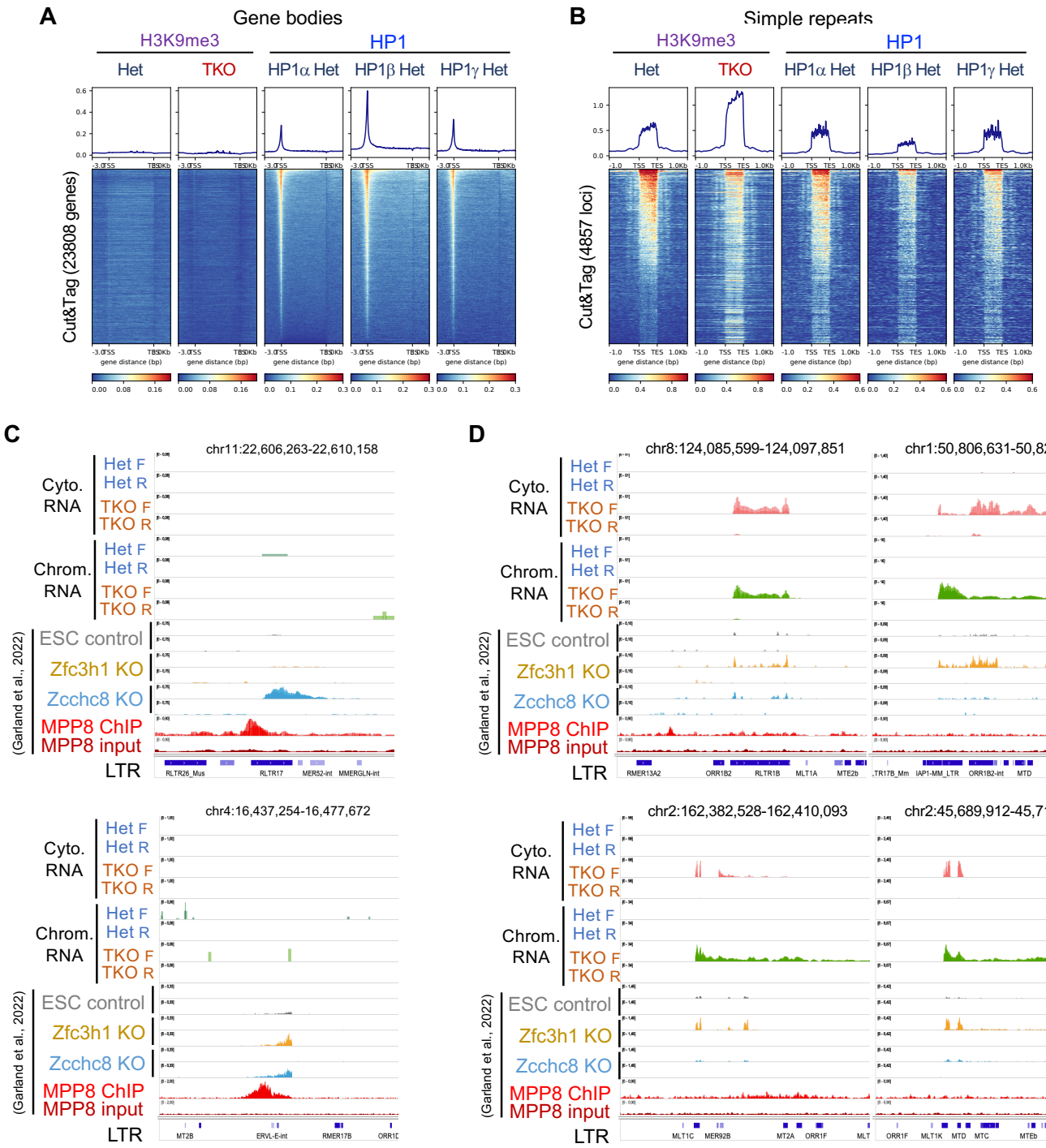

Supplementary Fig. 3: HP1/RNA Exosome loci and H3K9me3 and MPP8 components of the HUSH complex.
A, B. Heatmaps of densities of H3K9me3 or HP1 isoforms by Cut&Tag in Het or TKO as indicated, on gene bodies (A) as in figures 3D-F, or on a list of simple repeats (B) from Repeat Masker database. **C, D.** Genome views of transcriptomes in Het or TKO (examples depicted in figure 2H) compared with transcriptomes of mESC invalidated for the expression of *Zcchc8* KO (sky blue profiles) or *Zfc3h1* KO (yellow profiles) and control mESC (grey profiles), together with MPP8 chIPseq (red) and input (dark red) profiles (GSE178550; Garland et al., 2022). **C.** Genome views of two examples of MPP8 ChIPseq peaks with a coincidental RNA profile in mESC KO. No upregulated RNA was detectable at these loci in Het or TKO. **D.** Genome views of upregulated RNA (green and red) in TKO at LTR loci, with a coincidental upregulated RNA in mESC KO (yellow and sky blue). No MPP8 ChIPseq peak was detectable at these loci.

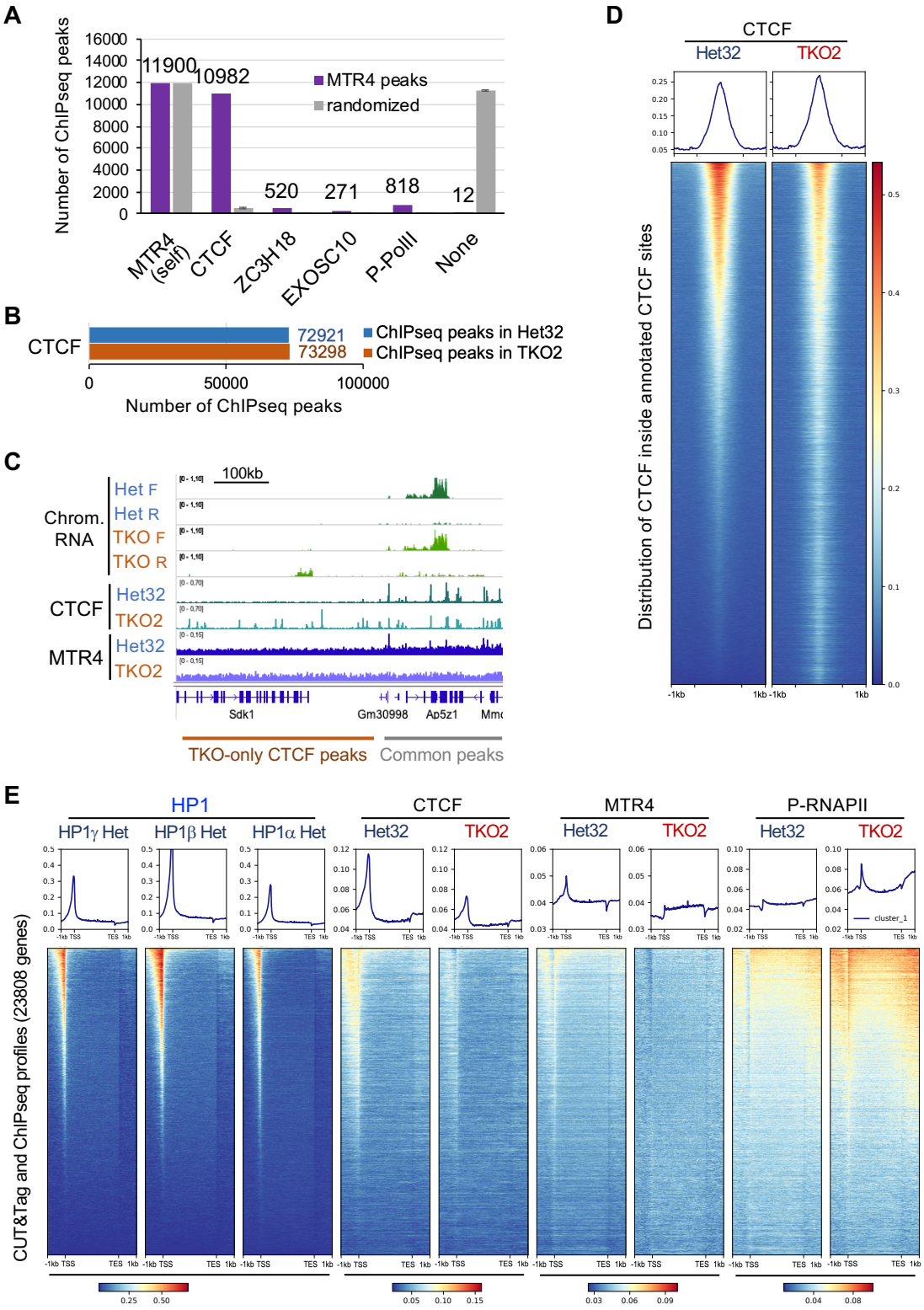

Fig. 4: HP1-dependent CTCF and MTR4 at promoters.
A. Number of MTR4 peaks (purple bars) colocalized with the other indicated ChIPseq peaks, compared to the same list of MTR4 peaks with randomized genomic locations (gray bars). **B,** Number of CTCF ChIPseq peaks versus IgG defined by MACS2 analysis in Het32 (blue) and TKO2 (brown). **C.** Genome view of chromatin-enriched RNA, CTCF and MTR4 densities at a locus showing two regions bearing TKO-only CTCF peaks (on the left), or peaks common to both cell types (on the right). **D.** Heatmaps of genome-wide CTCF ChIPseq densities in Het32 and TKO2 centered on all CTCF ChIPseq peaks. **E.** Heatmaps of ChIPseq densities of the indicated proteins on 23808 gene bodies defined as TSS to TES intervals, in Het32 (dark blue), in TKO2 (dark red).

Fig. 5

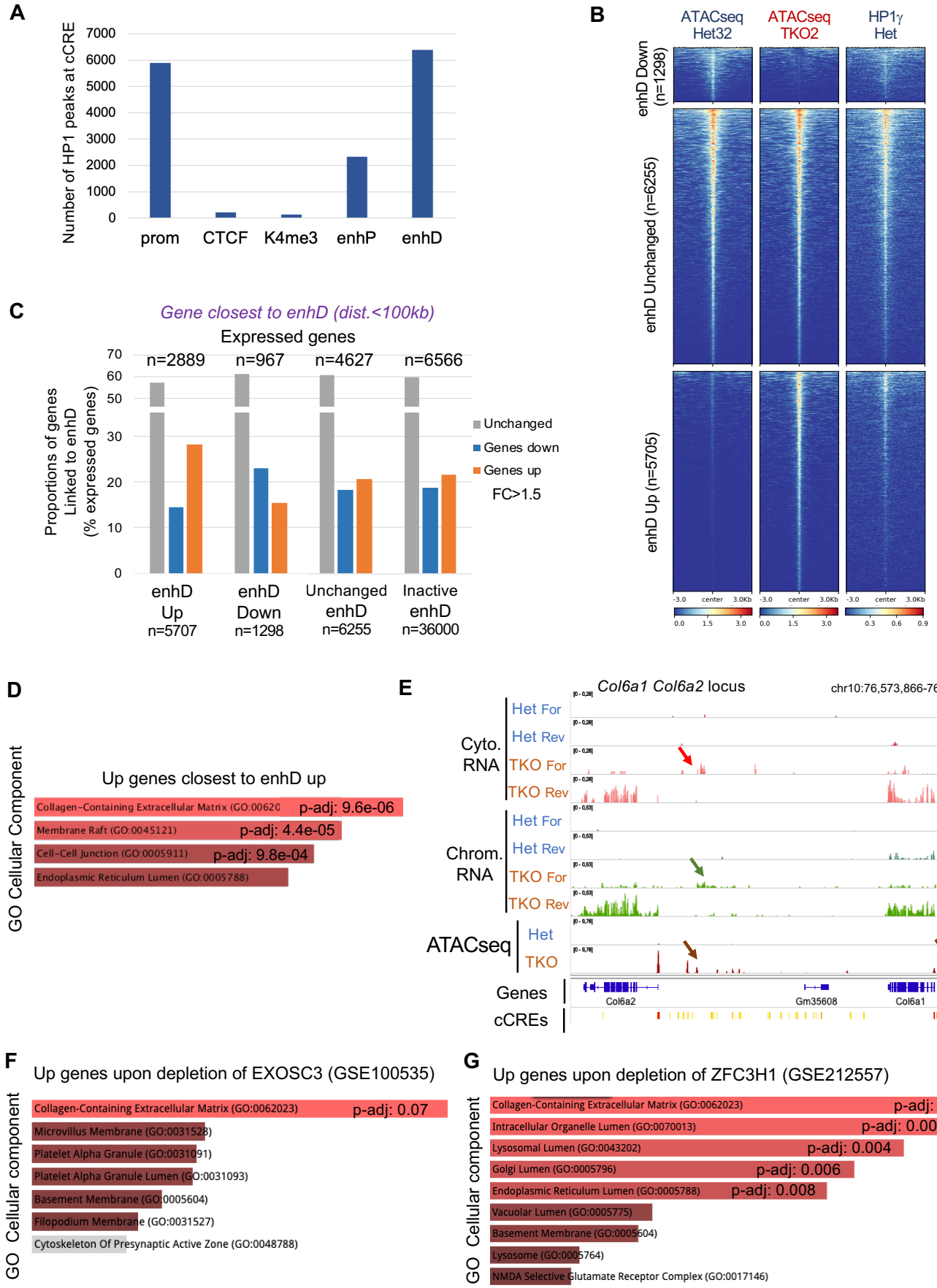
A
Number of HP1 peaks at cCRE
7000
6000
5000
4000
3000
2000
1000
0
prom
CTCF
K4me3
enhP
enhD
B
ATACseq Het32
ATACseq TKO2
HP1γ Het
enhD Down (n=1298)
enhD Unchanged (n=6255)
enhD Up (n=5705)
-3.0
center
3.0Kb
0.0
1.5
3.0
0.3
0.6
0.9
C
Gene closest to enhD (dist.<100kb)
Expressed genes
Proportions of genes Linked to enhD (% expressed genes)
n=2889
n=967
n=4627
n=6566
Unchanged
Genes down
Genes up
FC>1.5
enhD Up n=5707
enhD Down n=1298
Unchanged enhD n=6255
Inactive enhD n=36000
D
GO Cellular Component
Up genes closest to enhD up
Collagen-Containing Extracellular Matrix (GO:00620
p-adj: 9.6e-06
Membrane Raft (GO:0045121)
p-adj: 4.4e-05
Cell-Cell Junction (GO:0005911)
p-adj: 9.8e-04
Endoplasmic Reticulum Lumen (GO:0005788)
E
Col6a1 Col6a2 locus
chr10:76,573,866-76,841,436
Cyto. RNA
Chrom. RNA
ATACseq
Het For
Het Rev
TKO For
TKO Rev
Het
TKO
Genes
cCREs
Col6a2
Gm35608
Col6a1
F
Up genes upon depletion of EXOSC3 (GSE100535)
GO Cellular component
Collagen-Containing Extracellular Matrix (GO:0062023)
p-adj: 0.07
Microvillus Membrane (GO:0031528)
Platelet Alpha Granule (GO:0031091)
Platelet Alpha Granule Lumen (GO:0031093)
Basement Membrane (GO:0005604)
Filopodium Membrane (GO:0031527)
Cytoskeleton Of Presynaptic Active Zone (GO:0048788)
G
Up genes upon depletion of ZFC3H1 (GSE212557)
GO Cellular component
Collagen-Containing Extracellular Matrix (GO:0062023)
p-adj: 0.002
Intracellular Organelle Lumen (GO:0070013)
p-adj: 0.002
Lysosomal Lumen (GO:0043202)
p-adj: 0.004
Golgi Lumen (GO:0005796)
p-adj: 0.006
Endoplasmic Reticulum Lumen (GO:0005788)
p-adj: 0.008
Vacuolar Lumen (GO:0005775)
Basement Membrane (GO:0005604)
Lysosome (GO:0005764)
NMDA Selective Glutamate Receptor Complex (GO:0017146)

Fig. 5: Changes in chromatin accessibility at enhancers affect collagen gene expression.
A. Number of CUT&Tag HP1 merged peaks located at cCRE regulatory elements annotated as in Supp. Fig. 5A. **B.** Heatmaps of ATACseq densities in Het and TKO cells, and of HP1g CUT&Tag density in Het cells centered at cCRE enhD enhancer regulatory elements. EnhD were categorized based on their chromatin accessibility by ATACseq between Het and TKO. Categories are as follows: Down, with decreased accessibility in TKO cells; Unchanged, active in both conditions; Up, with increased accessibility in TKO cells; inactive (not shown), with no ATACseq density, respectively. **C.** Proportions of expressed genes in the closest proximity (within 100kb) to enhD in the categories depicted in 5B. Bars represent genes that were up- (orange) or down-regulated (blue) by more than 1.5 fold in TKO versus Het, or unchanged (grey). The total number of genes associated with each enhD category is indicated above the histogram. **D.** GO term analysis by enrichR associated with upregulated genes closest to upregulated enhD. **E.** Genome view of stranded chromatin-enriched (green) and cytosolic (red) RNA densities on the *Col6a1 Col6a2* locus, together with ATACseq densities in Het and TKO, showing TKO-specific ATACseq density (brown arrows) colocalizing with TKO-specific RNA (green and red arrows) and a group of enhD elements depicted in the cCRE lane. Yellow bars, enhD/enhP; red bars, Prom; blue bar, CTCF, as annotated in Supp.Fig. 5A. **F, G.** GO term analysis by enrichR associated with upregulated genes upon depletion of the indicated RNA exosome components.

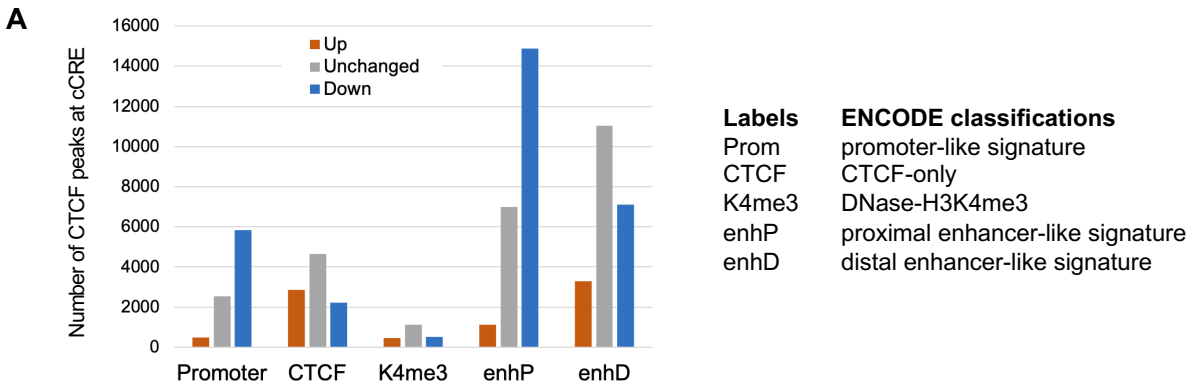

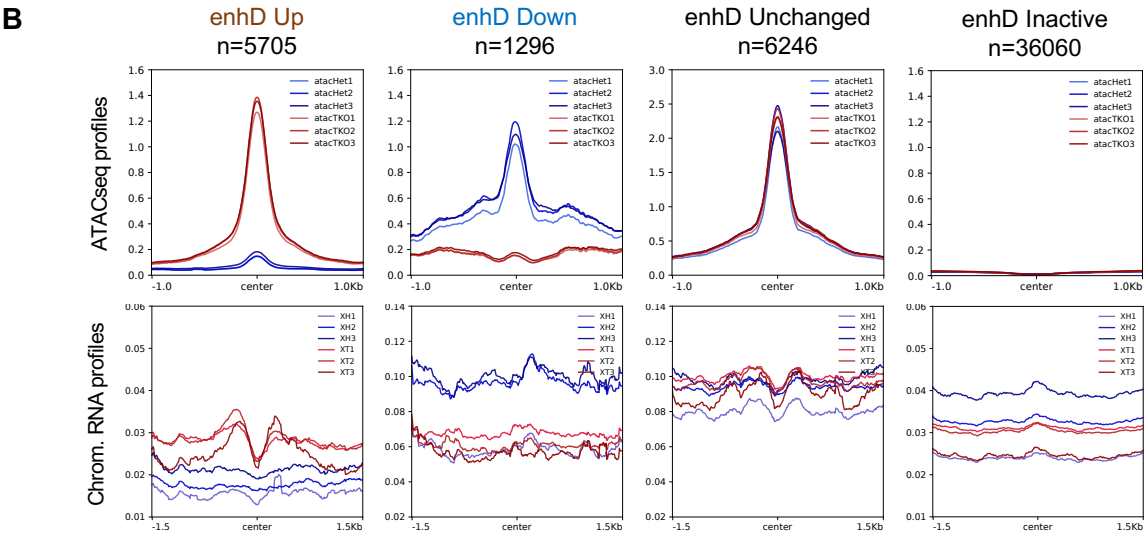

C

Collagen Transcriptome TKO vs Het (DESeq2)

Gene name	BaseMean	log2FC	adj-pVal	
Col1a1	26	2.25	4.98E-02	*
Col2a1	62	5.86	2.54E-05	***
Col4a1	4191	0.31	9.29E-01	
Col4a2	2231	0.16	9.67E-01	
Col4a4	34	1.28	7.31E-01	
Col4a5	1575	-0.80	8.08E-01	
Col5a1	939	0.77	9.10E-01	
Col6a1	38	3.94	1.02E-02	*
Col6a2	45	7.51	9.37E-05	****
Col6a3	43	4.22	1.91E-06	****
Col7a1	153	1.62	7.91E-02	
Col9a3	112	0.42	8.16E-01	
Col11a2	311	-0.06	9.92E-01	
Col12a1	91	-1.61	3.88E-01	
Col15a1	144	-1.22	3.15E-01	
Col16a1	57	4.01	2.66E-04	****
Col17a1	14	1.34	6.46E-01	
Col18a1	2373	0.38	7.94E-01	
Col20a1	300	0.68	8.62E-01	
Col24a1	36	0.62	8.92E-01	
Col27a1	198	2.28	3.91E-02	*

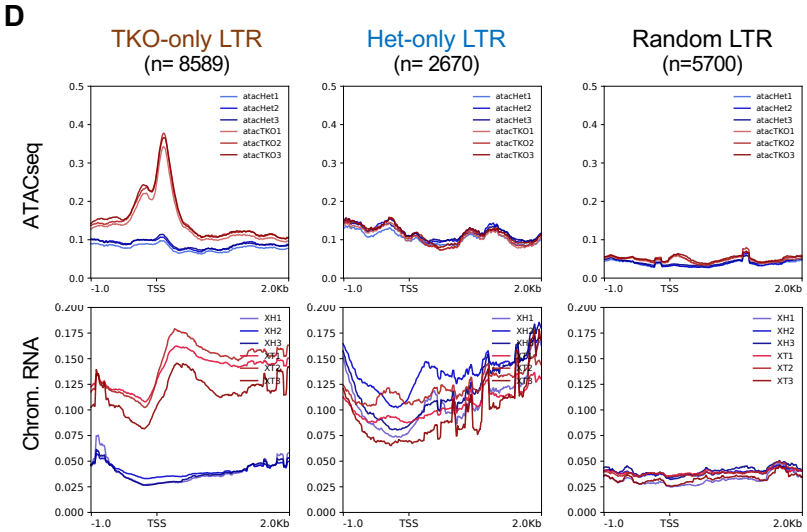

Supplementary Fig. 5: ATACseq and chromatin-associated RNA at enhancers and LTRs.
A. Number of CTCF ChIPseq peaks located at the cCRE regulatory elements labelled according to the ENCODE cCRE classifications (right panel). Bars represent CTCF peaks that were up- (brown) or down-regulated (blue) by more than 2 fold in TKO versus Het, or changed by less than 20 percent (Unchanged, grey). **B.** Average density profiles on enhD elements. Top panels, ATACseq profiles, and bottom panels, chromatin-associated RNA density profiles in triplicate Het (blue profiles) and TKO (red profiles) samples on enhD elements in the cCRE ENCODE database. EnhD were categorized based on their chromatin accessibility by ATACseq between Het and TKO. Categories are as follows: Down, with decreased accessibility in TKO cells; Unchanged, active in both conditions; Up, with increased accessibility in TKO cells; inactive, with no ATACseq density, respectively. **C.** List of Collagen genes dysregulated in Het versus TKO by DESeq2 analysis. Base mean is their mean expression levels in both Het and TKO, log2FC is the fold change in TKO versus Het, with adjusted p-values. **D.** Average density profiles on LTR retroelements. Top panels, ATACseq profiles, and bottom panels, chromatin-associated RNA density profiles in triplicate Het (blue profiles) and TKO (red profiles) samples. TKO-only LTRs and Het-only LTRs correspond to the categories of extragenic expressed LTRs depicted in Fig. 2B. Random LTR is a subset of 5,700 LTR elements in the Repat Masker database chosen randomly.

Fig. 6

A

Group	Patient	CBX1	CBX3	CBX5	Total HP1	MO	Survival
Hi HP1	11	26.58	51.31	20.11	98	MO4	Deceased
Hi HP1	13	15.16	38.15	26.88	80.19	MO3	Deceased
Hi HP1	18	31.07	35.9	6.253	73.223	MO2	Deceased
Hi HP1	1	11.98	52.04	3.303	67.323	MO4	Deceased
Hi HP1	20	23.36	52.33	21.89	97.58	MO4	Deceased
Hi HP1	21	59.8	33	30.24	123.04	MO4	Deceased
Hi HP1	30	43.82	59.86	41.78	145.46	MO1	Deceased
Hi HP1	3	31.47	43.53	8.316	83.316	MO4	Deceased
Hi HP1	40	17.39	56.2	9.783	83.373	MO3	Alive
Hi HP1	51	26.22	34.83	13.47	74.52	MO1	Alive
Hi HP1	53	19.59	63.39	22.81	105.79		Deceased
Hi HP1	55	9.006	39.34	16.46	64.806	MO1	Alive
Hi HP1	61	65.77	70.46	57.78	194.01	MO4	Alive
Hi HP1	63	33.45	47.16	4.397	85.007		
Hi HP1	65	11.07	60.54	15.2	86.81	MO4	Alive
Hi HP1	66	21.23	57.28	13.82	92.33	MO1	Alive
Hi HP1	67	28.14	45.95	31.22	105.31	MO3	Deceased
Hi HP1	9	25.42	28.98	8.282	62.682	MO4	Alive
Lo HP1	12	5.745	11.64	6.431	23.816	MO2	Alive
Lo HP1	17	2.253	4.912	2.557	9.722	MO1	Alive
Lo HP1	26	3.459	9.933	5.034	18.426	MO1	Alive
Lo HP1	28	3.673	5.533	4.079	13.285	MO2	Alive
Lo HP1	29	2.874	9.668	4.793	17.335	MO3	Deceased
Lo HP1	2	5.678	13.82	6.402	25.9	MO3	Alive
Lo HP1	32	2.295	7.094	1.152	10.541	MO3	Deceased
Lo HP1	34	3.079	11.32	3.245	17.644	MO1	Alive
Lo HP1	35	3.109	7.974	3.899	14.982	MO2	Alive
Lo HP1	36	6.416	11.13	7.147	24.693	MO2	Alive
Lo HP1	44	3.712	10.44	3.583	17.735	MO4	Alive
Lo HP1	45	3.535	13.14	2.123	18.798	MO1	Alive
Lo HP1	46	0.9888	2.456	0.8371	4.2819	MO2	Alive
Lo HP1	47	1.051	8.005	1.257	10.313		Deceased
Lo HP1	52	7.036	11.39	2.564	20.99	MO4	Alive
Lo HP1	56	1.514	5.67	1.838	9.022	MO1	Alive
Lo HP1	58	1.272	3.102	1.945	6.319	MO3	Alive
Lo HP1	59	0.7354	7.267	0.188	8.1904	MO1	Deceased

B

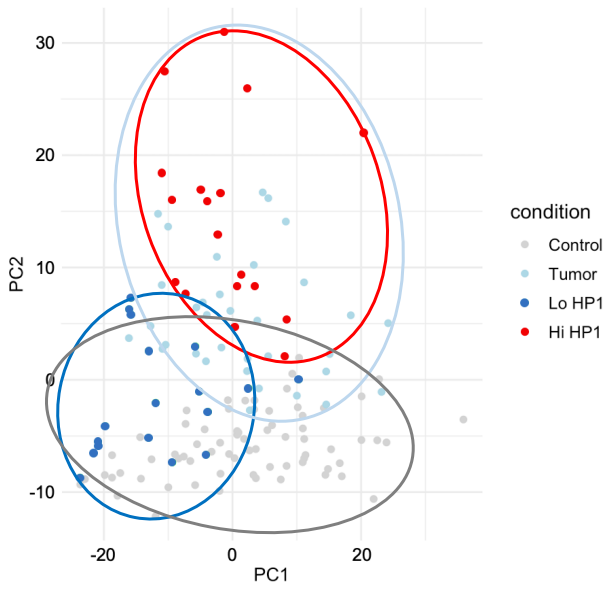

C

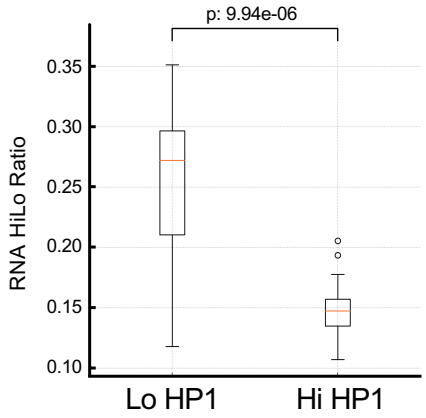

D

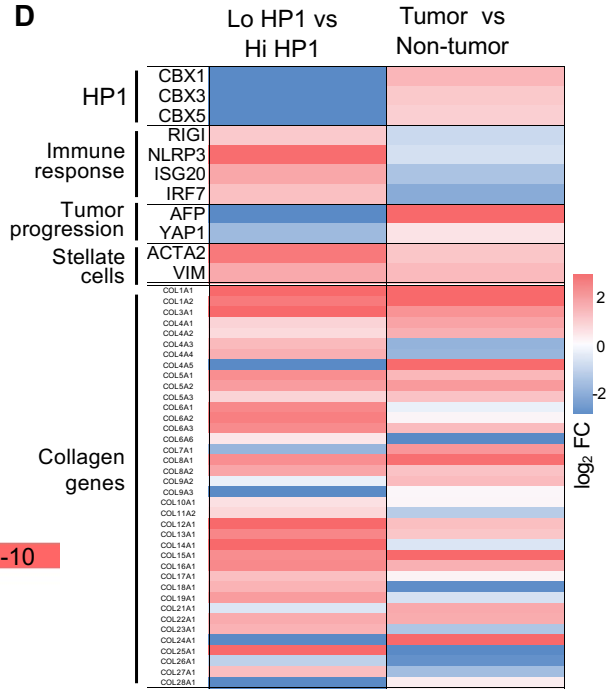

E

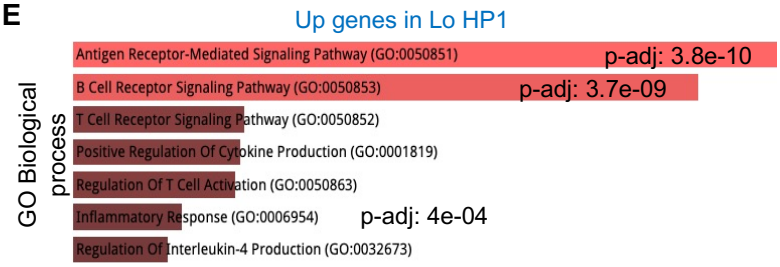

F

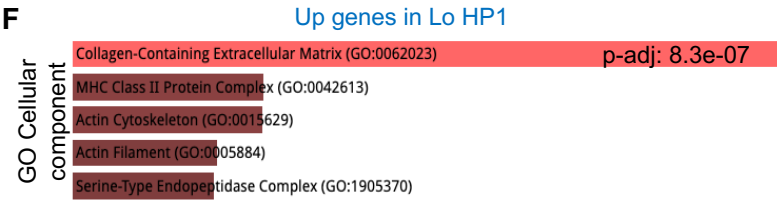

G

	Hi HP1 tumors	Lo HP1 tumors
HP1 expression	High	Low
Proliferation	High	Low
Immune response	Low	High
Mortality	High	Lower
Collagen expression	High	**Higher**

Fig. 6: HP1 expression affects collagen genes in hepatocellular carcinoma (HCC) patient samples.
A. Table of patient ranking in high HP1 (Hi HP1) and Low HP1 (Lo HP1) expressing samples based on their cumulative total HP1 expression levels, and compared with gene expression of individual HP1 isoforms. Molecular subclasses (MO) sorted by increasing severity of the disease from MO1 to MO4, and patient survival criteria have been analyzed in Candia *et al.*, 2020. **B.** Unsupervised PCA analysis of patient samples. **C.** Quantification of the accumulation of unstable mRNAs in Lo HP1 and Hi HP1 groups using the RNA HiLo ratio analysis as in ref. [48]. ***, p-value : 9.94E-06 (two-tailed Student's t-test). **D.** Heatmaps of log2 fold changes in expression of genes representative of tumor properties indicated as categories on the left and described in the main text, in Lo HP1 versus Hi HP1 tumor samples (left) and in tumor versus matching non-tumor samples (right). Log2 FC were obtained by DESeq2 analysis. **E, F.** Histograms of the most significant indicated Gene Ontology (GO) terms and their adjusted p-values for upregulated genes in Lo HP1 patient samples. **G.** Summary of tumor characteristics in the Hi and Lo HP1 groups.

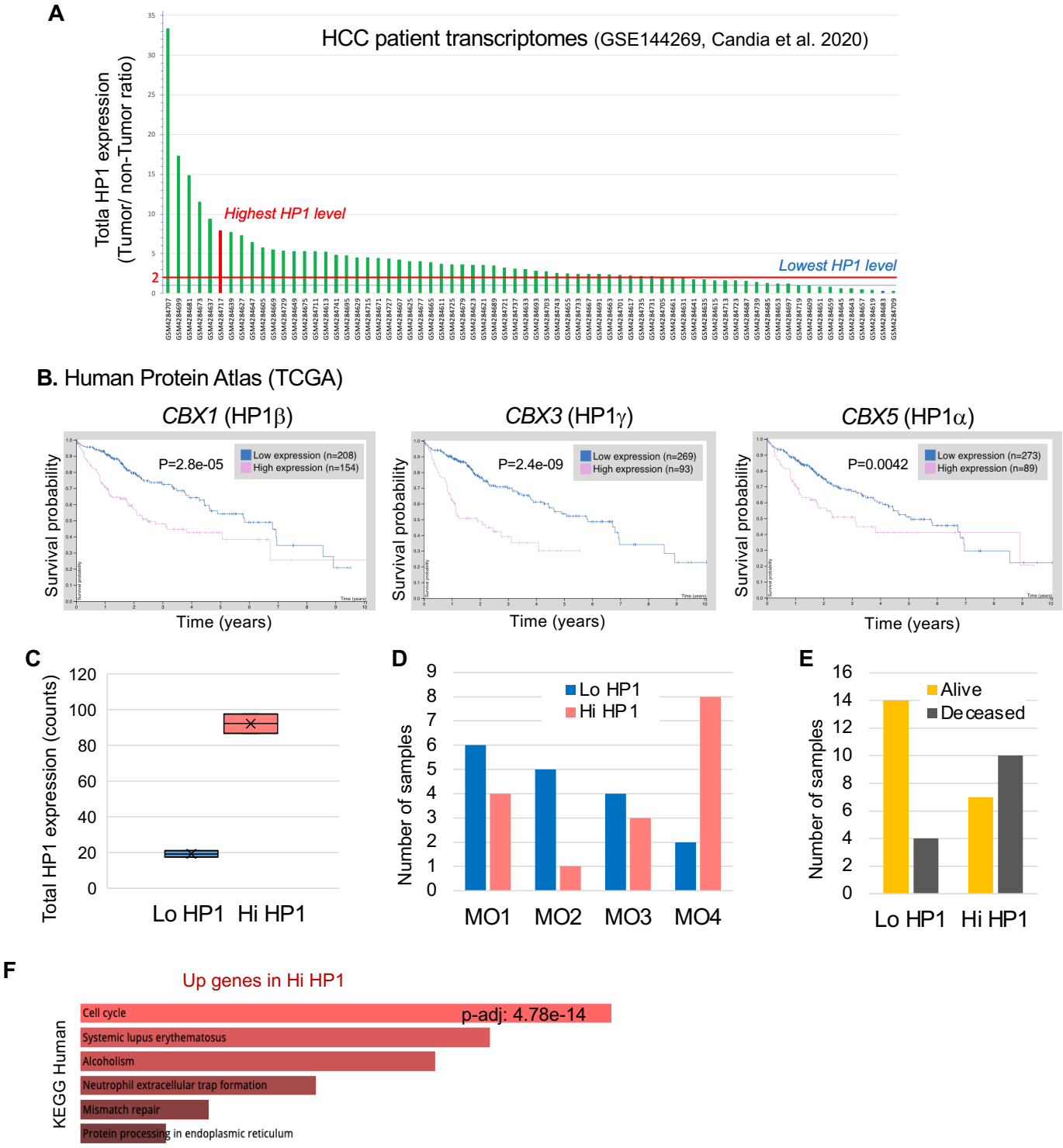

Supplementary Fig. 6: Metadata associated with the analysis of HCC patient samples.
A, Histogram of total HP1 expression ratio in tumors relative to adjacent non-tumor samples of 76 HCC patient transcriptomes (GSE144269, ref. 47) **B.** Kaplan-Meyer plots of liver cancer patient survival probabilities associated with *CBX1* (HP1b), *CBX3* (HP1g), and *CBX5* (HP1a) from the. Survival curves for low expression (blue) are compared to high expression (pink) of the indicated genes. P scores indicate log-rank P values of correlation between expression levels and patient survival. **C.** Total HP1 expression levels in the two groups of high HP1 (Hi HP1) and Low HP1 (Lo HP1) patients defined by the first and third total HP1 expression quartiles, respectively, related to Fig. 6A. **D, E,** Histograms of the number of Hi HP1 and Lo HP1 patients clustered according to four Molecular subclasses (MO) sorted by increasing severity of the disease from MO1 to MO4 (D), or showing survival criteria (E), as defined in ref. 47. **F.** Histograms of the most significant KEGG (Kyoto Encyclopedia of Genes and Genomes) pathways corresponding to upregulated genes in Hi HP1, sorted by adjusted p-values.